



**UNIVERSIDAD DE INVESTIGACIÓN DE TECNOLOGÍA
EXPERIMENTAL YACHAY**

Escuela de Ciencias Físicas y Nanotecnología

**TÍTULO: Production of Polytetrafluoroethylene Nanoparticles:
Towards the Design of Bio-functional Nanoparticles**

Trabajo de integración curricular presentado como requisito para la
obtención del título de Ingeniero en Nanotecnología

Autor:

Chingo Aimacaña Cristhian Marcelo

Tutor:

P.h.D. Dahoumane Si Amar

Urcuquí, agosto 2019

Urcuquí, 28 de agosto de 2019

SECRETARÍA GENERAL
(Vicerrectorado Académico/Cancillería)
ESCUELA DE CIENCIAS FÍSICAS Y NANOTECNOLOGÍA
CARRERA DE NANOTECNOLOGÍA
ACTA DE DEFENSA No. UITEY-PHY-2019-00022-AD

En la ciudad de San Miguel de Urcuquí, Provincia de Imbabura, a los 28 días del mes de agosto de 2019, a las 17:00 horas, en el Aula Sala Capitular de la Universidad de Investigación de Tecnología Experimental Yachay y ante el Tribunal Calificador, integrado por los docentes:

Presidente Tribunal de Defensa	Dr. CHACON TORRES, JULIO CESAR , Ph.D.
Miembro No Tutor	Dra. LOPEZ GONZALEZ, FLORALBA AGGENY , Ph.D.
Tutor	Dr. DAHOUMANE , SI AMAR , Ph.D.

Se presenta el(la) señor(ita) estudiante **CHINGO AIMACAÑA, CRISTHIAN MARCELO**, con cédula de identidad No. 1727584664, de la **ESCUELA DE CIENCIAS FÍSICAS Y NANOTECNOLOGÍA**, de la Carrera de **NANOTECNOLOGÍA**, aprobada por el Consejo de Educación Superior (CES), mediante Resolución **RPC-SO-13-No.156-2015**, con el objeto de rendir la sustentación de su trabajo de titulación denominado: **Production of Polytetrafluoroethylene Nanoparticles: Towards the Design of Bio-functional Nanoplatforms**, previa a la obtención del título de **INGENIERO/A EN NANOTECNOLOGÍA**.

El citado trabajo de titulación, fue debidamente aprobado por el(los) docente(s):

Tutor _____ Dr. DAHOUMANE , SI AMAR , Ph.D.

Y recibió las observaciones de los otros miembros del Tribunal Calificador, las mismas que han sido incorporadas por el(la) estudiante.

Previamente cumplidos los requisitos legales y reglamentarios, el trabajo de titulación fue sustentado por el(la) estudiante y examinado por los miembros del Tribunal Calificador. Escuchada la sustentación del trabajo de titulación, que integró la exposición de el(la) estudiante sobre el contenido de la misma y las preguntas formuladas por los miembros del Tribunal, se califica la sustentación del trabajo de titulación con las siguientes calificaciones:

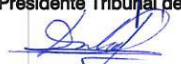
Tipo	Docente	Calificación
Presidente Tribunal De Defensa	Dr. CHACON TORRES, JULIO CESAR , Ph.D.	10,0
Miembro Tribunal De Defensa	Dra. LOPEZ GONZALEZ, FLORALBA AGGENY , Ph.D.	9,8
Tutor	Dr. DAHOUMANE , SI AMAR , Ph.D.	10,0

Lo que da un promedio de: **9.9 (Nueve punto Nueve)**, sobre 10 (diez), equivalente a: **APROBADO**

Para constancia de lo actuado, firman los miembros del Tribunal Calificador, el/la estudiante y el/la secretario ad-hoc.


CHINGO AIMACAÑA, CRISTHIAN MARCELO
Estudiante


Dr. CHACON TORRES, JULIO CESAR , Ph.D.
Presidente Tribunal de Defensa


Dr. DAHOUMANE , SI AMAR , Ph.D.
Tutor



Dra. LÓPEZ GONZÁLEZ, FLORALBA AGGENY , Ph.D.
Miembro No Tutor



CIFUENTES TAFUR, EVELYN CAROLINA
Secretario Ad-hoc

Autoría

Yo, **CRISTHIAN MARCELO CHINGO AIMACAÑA**, con cédula de identidad 172758466-4, declaro que las ideas, juicios, valoraciones, interpretaciones, consultas bibliográficas, definiciones y conceptualizaciones expuestas en el presente trabajo; así cómo, los procedimientos y herramientas utilizadas en la investigación, son de absoluta responsabilidad de el/la autora (a) del trabajo de integración curricular. Así mismo, me acojo a los reglamentos internos de la Universidad de Investigación de Tecnología Experimental Yachay.

Urcuquí agosto 2019.



Cristhian Marcelo Chingo Aimacaña

CI:172758466-4

Autorización de Publicación

Yo, **CRISTHIAN MARCELO CHINGO AIMACAÑA**, con cédula de identidad 172758466-4, cedo a la Universidad de Tecnología Experimental Yachay, los derechos de publicación de la presente obra, sin que deba haber un reconocimiento económico por este concepto. Declaro además que el texto del presente trabajo de titulación no podrá ser cedido a ninguna empresa editorial para su publicación u otros fines, sin contar previamente con la autorización escrita de la Universidad.

Asimismo, autorizo a la Universidad que realice la digitalización y publicación de este trabajo de integración curricular en el repositorio virtual, de conformidad a lo dispuesto en el Art. 144 de la Ley Orgánica de Educación Superior

Urcuquí, agosto 2019.



Cristhian Marcelo Chingo Aimacaña

CI:172758466-4

Dedicatoria

A mis queridos padres por haberme apoyado y motivado constantemente durante mi proceso de formación para finalmente alcanzar mis anhelos.

Cristhian Marcelo Chingo Aimacaña

Acknowledgements

This project is presented as the last step to glean the college degree, whose development was made thanks to several people. I am grateful for a number of professors, friends, and colleagues, whose encouragement, support, and assistance, boosted me to finalize it. In Yachay Tech (Urcuquí, Ecuador), I was constantly guided by my advisor Si Amar Dahoumane, whose support was essential for handling and overcoming adversities. Furthermore, I sincerely thank my co-advisor Jose Luis Cuevas as well as Frank Alexis, Juan Pablo Saucedo, and Thibault Terencio for their patience and continued support. I also thank laboratory technicians whose advice and experience guided me during trials in the laboratory. In ESPE (Sangolquí, Ecuador), I would like to acknowledge with gratitude to Alexis Debut, who has aided me to get wonderful final results. In Clemson University (SC 29634 USA), I thank Daniel C. Whitehead & Mohammed Attia for helping me with sample characterization. My closest friends in the University also support and encourage me to be better, they are: Cristhian Proaño, Byron Tipan, and Vanessa Hinojosa. Finally, I thank my parents: Margarita Aimacaña and Jorge Chingo; and my siblings: Mónica and Carlos for making everything possible.

Cristhian Marcelo Chingo Aimacaña

Resumen

Las fascinantes propiedades mostradas por el politetrafluoroetileno (PTFE) han atraído la atención de los científicos, ya que este material ha encontrado varias aplicaciones en el campo biomédico. Algunos estudios han resaltado el potencial del PTFE en la atenuación por ultrasonido (US). El presente trabajo tiene como objetivo sintetizar nanopartículas (NPs) de PTFE y caracterizarlas como nuevas nanoplataformas para el tratamiento de la hipertermia del cáncer. Estas NPs de PTFE se obtuvieron dispersando sellador de teflón en una mezcla de ácido fluorhídrico (HF) y etanol, seguido de sonicación y centrifugación diferencial antes de estabilizarlos en polisorbato-80 (Tween-80). Esto produjo una población bimodal de NPs de PTFE de 14 nm y 105 nm de tamaño promedio, como se muestra en las imágenes de Microscopía Electrónica de Transmisión (TEM). Además, se utilizaron espectroscopía infrarroja con transformada de Fourier (FTIR), difracción de rayos-X (XRD) y espectroscopía visible ultravioleta de reflectancia difusa (UV-Vis) para caracterizar aún más las NPs producidas. Por ejemplo, XRD muestra picos debido a la presencia de NPs de PTFE además de picos de contaminación identificada como rutilo. Además, las NPs de PTFE han demostrado su potencial en imagen de rayos X y US. En última instancia, la perspectiva del PTFE en el campo médico se presenta para teragnosis de cáncer.

Palabras Clave: NPs de PTFE, Síntesis, Estabilidad Coloidal, Caracterización, Propiedades Biomédicas, Imágenes, Teragnosis

Abstract

Fascinating properties shown by polytetrafluoroethylene (PTFE) have attracted the attention of scientists as this material has found several applications in the biomedical field. Some studies have highlighted the potential of PTFE in ultrasound (US) attenuation. The present work aims at synthesizing PTFE nanoparticles (NPs) and characterizing them as new nanoplatforms for the hyperthermia treatment of cancer. These PTFE NPs were obtained by dispersing Teflon sealant in a mixture of hydrofluoric acid (HF) and ethanol, followed by sonication and differential centrifugation before being stabilized in polysorbate 80 (Tween-80). This yielded bimodal population of PTFE NPs of 14 nm and 105 nm in average size as displayed by Transmission Electron Microscopy (TEM) images. Additionally, Fourier-Transform Infrared spectroscopy (FTIR), X-ray diffraction (XRD) and diffuse reflectance ultraviolet visible spectroscopy (UV-Vis) were used to further characterize the as-produced PTFE NPs. For instance, XRD displays peaks due to the presence of PTFE NPs in addition to peaks from contamination with rutile. Moreover, the PTFE NPs have shown their potential in X-ray and US imaging. Ultimately, the outlook of PTFE in the medical field is presented for cancer theranostics.

Keywords: PTFE NPs, Synthesis, Colloidal Stability, Characterization, Biomedical Properties, Imaging, Theranostics.

Contents

List of Figures	xi
List of Tables	xiii
List of Papers	xiv
1 Introduction	1
1.1 Literature Review	1
1.1.1 What is Cancer?	1
1.1.2 Conventional and Emerging Cancer Treatments	3
1.1.3 What is PTFE?	11
1.1.4 Ultrasound in Medicine	16
1.1.5 The Behavior of Teflon® Under Ultrasound	17
1.2 Problem Statement	19
1.3 General and Specific Objectives	20
2 Methodology	21
2.1 Synthesis of PTFE Fine-powder and NPs	21
2.1.1 Sonication	22
2.1.2 Differential Centrifugation to Separate NPs per Size	23
2.2 Characterization of PTFE	25

2.2.1	Diffuse Reflectance Ultraviolet Visible (UV-Vis) Spectroscopy	25
2.2.2	X-ray Powder Diffraction	28
2.2.3	X-ray Imaging	29
2.2.4	Ultrasound Imaging	30
2.2.5	Transmission Electron Microscopy	31
2.2.6	Fourier Transform Infrared Spectroscopy	32
3	Results & Discussion	35
3.1	Synthesis of PTFE Fine-powder and NPs	35
3.1.1	Production of PTFE Fine-powder	35
3.1.2	Production of PTFE NPs	37
3.2	Characterization of PTFE Fine-powder and NPs	39
3.2.1	Diffuse Reflectance UV-Vis Spectroscopy of PTFE Fine-powder	39
3.2.2	X-ray Powder Diffraction of PTFE Fine-powder	41
3.2.3	X-ray Imaging of PTFE Fine-powder	49
3.2.4	Ultrasound Imaging of PTFE Fine-powder	50
3.2.5	Transmission Electron Microscopy of PTFE NPs	51
3.2.6	Fourier Transform Infrared Spectroscopy of PTFE NPs	54
4	Conclusions & Outlook	58
4.1	Conclusions	58
4.2	Outlook	60
A.1	Abbreviations	62
	Bibliography	65

List of Figures

1.1	Proliferation of Cancer Cells With Altered Configuration of the Chromosome.	2
1.2	Incidence of Cancer in Male and Female Ecuadorian Population During 2010-2014.	4
1.3	Ways in Which Hyperthermia is Performed for Local and Global Treatment.	7
1.4	Regulation of cellular processes by size-dependent gold nanoparticles (GNPs) on breast cancer.	10
1.5	PTFE Structure Showing the C-F Chains and Conformation of the Unit Cell.	11
1.6	Illustrative Sketch of Sound Frequencies.	16
1.7	Attenuation of Ultrasound by a PTFE Tube of 4.75 mm of Thick.	18
2.1	Graphical Description of the Process of Cavitation Produced into the Liquid Phase due to Waves of Ultrasound and Ways to Produce the Sonication of the Samples.	23
2.2	Process of Differential Centrifugation.	24
2.3	Optical Phenomena Produced During Diffuse Reflectance in Powder Samples.	27
2.4	Interaction of Sample and X-rays During XRD Analysis and the Relation With Bragg's law.	28
2.5	Schematic Representation of a TEM Device.	31
2.6	Michelson Interferometer that Converts a Incoming Infrared Beam into Interference Wave that Interacts With the Sample	33
3.1	Implements and Methodology Employed in the Synthesis of PTFE Fine-powder.	37
3.2	Implements Employed in the Production of PTFE NPs from Fine-powder	38
3.3	Instruments Used for the Diffuse Reflectance UV-Vis Analysis of PTFE Fine-powder.	41

3.4	Diffuse Reflectance Spectroscopy Spectrum of PTFE Fine-powder.	42
3.5	FTIR Spectrum for PTFE NPs in Colloidal Solution of Ethanol, and Tween-80.	43
3.6	Unit cell of PTFE Packaged by chains of CF ₂ in a hexagonal lattice. Additionally, the unit cell is Repeated with the main Planes in order to Compare With the Peaks of XRD pattern.	46
3.7	Phase Diagram of PTFE For different Temperatures and Pressures.	47
3.8	X-ray Imaging of PTFE Fine-powder.	49
3.9	Ultrasound Imaging of PTFE Fine-powder.	50
3.10	TEM Images of PTFE NPs in Colloidal Dispersion Prior to Differential Centrifuging.	52
3.11	TEM Images of PTFE NPs in Colloidal Solution After Differential Centrifuging.	53
3.12	FTIR spectrum of NPs in Colloidal Dispersion of ethanol, and Tween-80.	56

List of Tables

1.1	Sonosensitizers Employed in Sonodynamic Therapy With Their Corresponding Conditions and Cells Treated.	9
1.2	List of Main Properties of PTFE	14
2.1	Advantages and Disadvantages of Ultrasound Imaging in Comparison with other Modalities Such as X-ray Computed Tomography (CT), Radionuclide Emission Tomography, and Magnetic Resonance Imaging (MRI)	30
3.1	Values Computed With the Fitting of UV-Vis Spectrum of PTFE Fine-powder	39
3.2	Description of Peaks Observed in the XRD Pattern for PTFE with Their Corresponding Miller Indexes, Interplanar Space, Position, and Relative Intensities With Respect to the More Intense peak (100).	44
3.3	Description of Peaks Observed in the XRD Pattern for PTFE with Their Corresponding Miller Indexes, Interplanar Space, Position, and Relative Intensities With Respect to the More Intense Peak (100).	46
3.4	Correlations Between Diffraction Peak Aberrations, Broadening, Shifts or Asymmetries, and the Different Elements of Microstructure.	48
3.5	Size Distribution of PTFE NPs Analyzed in Figures 3.10 (Before Centrifuging) and 3.11 (After Centrifuging).	51
3.6	Frequencies (cm^{-1}) of Main Peaks Observed in the FTIR spectrum With Their Corresponding Vibrational Modes.	55

Chapter 1

Introduction

1.1 Literature Review

1.1.1 What is Cancer?

Cancer is the name given to a bunch of linked diseases caused by the abnormal growth of cells¹. Cancer cells exhibit alterations in the chromosomes produced by inheritance from parents or by a sudden damage in the deoxyribonucleic acid (DNA). It is well-known that a chromosome consists of DNA coiled around proteins that support the structure². Disturbances in DNA occur in two ways: spontaneously or induced. In one hand, spontaneous mistakes are produced during DNA replication due to the chemical instability of purine and pyrimidine bases. On the other hand, when an organism is exposed to environmental factors, such as ultraviolet light or chemical carcinogens, DNA mutations are produced³. Changes in DNA, known as mutations, induce a euploid karyotic state in chromosomes. In this state, the altered genetic configuration is responsible for uncontrolled cell growth and division that, subsequently, produces malignant tumors. Mutations are inherited by the other cells during the process of cellular division where the altered chromosomes are replicated, as shown in Fig 1.1. Genetic changes responsible for DNA mutations are random within a single tumor, this means each malignant tumor is unique for each patient⁴.

Cancer can not be developed autonomously as it needs the interconnection of multiple cell types. Fibroblasts, epithelial cells, innate and adaptive immune cells, blood and lymphatic cells, and specialized mesenchymal cell types are involved in the onset of cancer. Additionally, mutant cells exploit the normal mechanism of the host to enhance the cancer development⁵. It is important to differentiate between benign

and malignant tumors. On one hand, benign tumors in most of the cases do not cause death as they do not spread to adjacent tissues. On the other hand, malignant tumors are dangerous; they spread out to the body through a process called metastasis and cause death if not treated¹.

Cancer and normal cells are different during cell division as a consequence of mutations. The division of normal cells is delimited by intrinsic and extrinsic factors, which induce a controlled duplication. On the contrary, the division of cancer cells is not proper as this process is not controlled yielding the formation of tumors. Usually, cells induce apoptosis to themselves when there are damages or inappropriate surroundings; however, cancer cells exhibit a disturbed lifetime being also stronger in presence of damages thus extending their lifespan.⁶

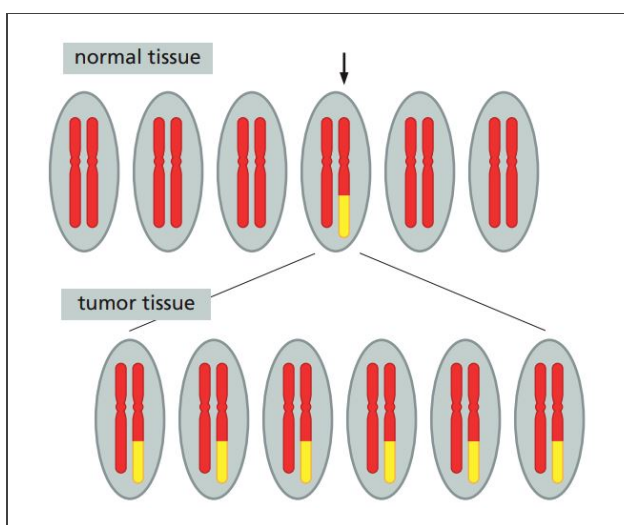


Figure 1.1: Proliferation of cancer cells with altered configuration of the chromosome. Copied from Ref. 1.

Cancer Statistics

Cancer is a worldwide dominant cause of death that is considered as the main barrier to increasing life expectancy at a global level⁷. In countries of low-resources, more than half of patients diagnosed with cancer die due to: (i) the limited access to resources for health, (ii) air pollution, and (iii) water contaminants among others⁸. In addition, in several countries of Latin America, such as Ecuador, cancer is the first or second leading cause of mortality for people under 70 years⁷.

The problem of health in the population is seriously treated with high delicacy, especially in populations from the Latin American region and other developing countries. For instance, Ecuador is a country with tremendous natural resources. The exploitation of these resources, such as oil (a main country income) impacts its environment negatively. Usually, the lands surrounding oil activities are highly contaminated, this can potentially affect the health of the nearby populations due to water contamination or fatal mistakes, like the oil dumping⁹. Studies about the incidence of oil activity in the cancer rates of nearby populations to oil wells have been carried out in Ecuador. This has been conducted in 4 provinces of the eastern region of Ecuador with a population of 356,406 inhabitants. Results showed a higher incidence of cancer, especially among children aged between 0 and 4 years who live in counties nearby to oil-development activities than those who live far away from any oil activity¹⁰.

Similarly, the World Health Organization (WHO) carried out a study regarding the incidence of cancer in the population of Ecuador for 2014 with a total population of 15,492,000. Cancer incidence was analyzed in two groups differentiating males and females using data about the most frequent types of cancer. The results provided by WHO demonstrated the high incidence of prostate cancer among males while the breast cancer predominated in females, as shown in Figure 1.2. Additionally, 14,025 cases of cancer were diagnosed in the whole Ecuadorian population in 2014; the detailed information is exhibited in Figure 1.2¹¹.

Furthermore, the cancer mortality was determined by comparing the total deaths registered during 2010-2014 with deaths related to cancer. The study of mortality was helpful to determine the percentage of people who died due to some types of cancer. This analysis showed that about 17% of 81000 registered deaths during 2010-2014 were caused by problems linked to cancer. Within the percentage of cancer mortality, females form the majority, cervix uteri cancer being the primary cause of death¹¹.

1.1.2 Conventional and Emerging Cancer Treatments

Efforts to improve cancer treatments had indeed led to the use of nanotechnology. Currently, Doxil and Abraxane, which have a diameter of 100 nm and 10 nm, respectively, are drugs based on nanotechnology that passed the regulatory scrutiny placing them already in the market¹². Cancer therapy has been improved by applying nanotechnology with the use of nanoparticles, that nowadays receive great attention¹³. Nonetheless, it is important to increase the knowledge on the biology of cancer and study conventional cancer treatments to propose more effective ways to combat this disease. Conventional cancer treatments are enlisted below:

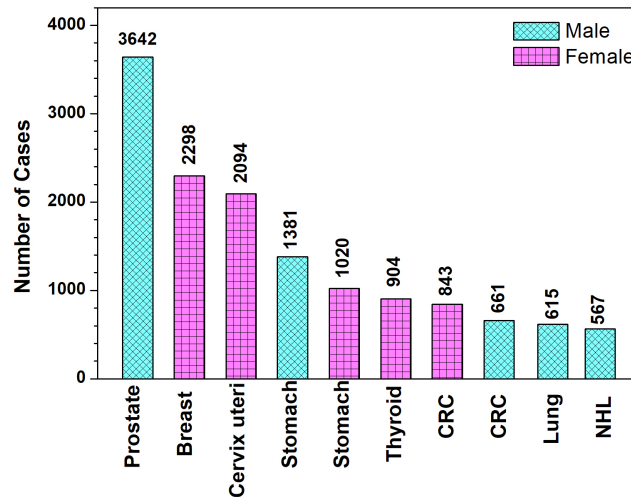


Figure 1.2: Incidence of cancer in male and female Ecuadorian population during 2010-2014. The x-axis shows the type of cancer, while the y-axis shows the number of cases observed for each type of cancer. Adapted from Ref. 11.

- **Surgery:** It is employed to prevent, diagnose or treat cancer. For example, the surgery is helpful against the proliferation of cancer when it is in advanced stages. Moreover, extracting a piece of tumor is favorable to debulk or determine the stage of the tumor¹⁴. In Ecuador, Sociedad de Lucha Contra el Cáncer (SOLCA), a society with the objective to combat cancer with highly specialized staff, offers surgery to treat various types of cancer¹⁵.
- **Radiotherapy:** This treatment is already used in Ecuador supported by the public health system. However, there are only 10 centers nationwide that offer this treatment and 28 radiation oncologists in charge of radiotherapy cures¹⁵. This technique consists in exposing the patient to high-energy particles or waves, such as X-rays, gamma rays, electron beams or protons, with the main objective to break the DNA molecules within the cancerous cells. The small fissures of DNA lead to cell death and the disappearance of the tumor.¹⁴.
- **Chemotherapy:** It is the use of potent drugs to kill cancer cells which have spread out from the primary tumor. Chemotherapy is used to make more effective a surgery or radiotherapy and in order to prevent the re-growth of the tumor¹⁴. This technique is also offered by public health centers in Ecuador¹⁵.

- **Targeted Cancer Therapy:** It is a recent technique similar to chemotherapy, but with more precision to attack and identify various types of cancer cells. This technique disrupts the normal cell-cycle affecting the DNA, because it dictates if the cell breed or die¹⁶. Targeted therapy is also offered in Ecuador: Quito, Guayaquil, and Cuenca being SOLCA main supplier of the drugs¹⁵.
- **Stem Cell Transplant:** The effectiveness of stem cell has been demonstrated in cancer therapy, for example the transplantation of bone marrow helps to regenerate the hematolymphoid system following myeloablative protocols. Commonly, this treatment is applied in cases when blood and immune system have been damaged in diseases, such as leukemia, lymphoma, or multiple myeloma¹⁷. In Ecuador, SOLCA started in 2006 a program of cancer combating with stem cell transplants¹⁵.
- **Immunotherapy:** The immune system acts against infections and destroys foreign targets. However malignant tumor immunity resistance has been demonstrated. The presence of a tumor indicates that the immune response did not detect the “danger”. It means that cancer promotes evasion of the immune system. For this reason, immunotherapy has been developed to help and stimulate the immune system in order to combat cancer¹⁸.
 - **Immune Checkpoint Inhibitors:** T and B cells are part of immune system, which are in charge to recognize antigens. However, their efficiency is very low at the moment to identify altered proteins or pathogens. For example, members of the immune system such as Cytotoxic T-Lymphocyte Associated Protein 4 (CTLA-4) are blockaded by using checkpoint inhibitors in order to promote T cells activation, proliferation, and anti-tumor response¹⁹.
 - **Therapy Targeting the Tumor Micro-environment:** There exist an interaction between immune cells and the tumor micro-environment, this relation safeguard the tumor from anti-cancer drugs. For example, monoclonal antibodies are employed to disrupt the signals that the immune system of the tumor produce to protect the tumor. For example, vaccines against human papiloma virus (HPV) helps to prevent cancer by targeting the micro-environment¹⁹.
 - **Oncolytic Virus Therapy:** Inside the cancer cells viruses replicates, whose genome is can be modified to enhance the T-cell activation. It is made with promoters, which modify the virus activity¹⁹.

Nowadays, there exist new treatment which use nanotechnology to enhance the treatment against cancer, for example hyperthermia:

Hyperthermia

It consists in increasing the temperature of the body over the normal 37.7 °C; some illnesses, such as fever, can increase the corporal temperature also. However, hyperthermia differs from illness because the increasing of the temperature is highly controlled to affect only cancer cells. When cancer cells are heated, they become more vulnerable to external factors due to changes happening inside²⁰.

During hyperthermia trials, the benign tumor is exposed to a temperature of about 43 °C for more than one hour. Additionally, it is well-known that the tumor is killed without damaging nearby healthy tissues when the temperature is in the range of 41 °C - 45 °C. This happens because cancer cells present high glycolytic activities making them highly acidic, which makes the cells susceptible to high temperatures, unlike the healthy cells²¹. Healthy cells are not affected by the high temperatures produced in hyperthermia as they are under thermoregulation. Thermoregulation occurs when the body increases the blood flow to about 20 times in the presence of high temperatures while this blood flow rises just the double in benign tumors. For this reason, cancer cells are further affected than healthy cells when hyperthermia is implemented²¹. In addition, molecular and biological mechanisms, such as membranes, the cytoskeleton, synthesis of macro-molecules and DNA repair are affected at high temperatures²². Preclinical experiments had demonstrated that the requirement of 43 °C is not indispensable; some experiments showed great efficacy even at lower temperatures. The response of cancer cells under the effect of temperature depends, additionally, on micro-environmental factors, such as the pH.

Multimodal oncological strategies are made with hyperthermia accompanied with other treatments, such as chemotherapy or radiotherapy, making the treatment more effective. Combining radiotherapy and hyperthermia is feasible to fight cancer effectively; however, it is not recommendable during medical trials. Different forms of energy, such as radio waves, microwaves, US waves, among others can produce thermal ablation. The main objective of hyperthermia is to induce high temperatures in an specific area of the body to affect exclusively cancer cells and avoid irreversible effects on healthy cells²².

This treatment could be focused for specific places to the whole body²⁰. Hyperthermia is used to increase the temperature of benign tumors achieving an homogeneous heat. The methods employed depend on the location of the tumor that are summarized below²².

- **Local hyperthermia:** It is used when superficial tumors are treated. Usually, this method employs commercial devices based on electromagnetic radiation, which are placed directly over the surface of the tumor²⁴.
- **Regional hyperthermia and part-body hyperthermia:** An array of antennas are used when the

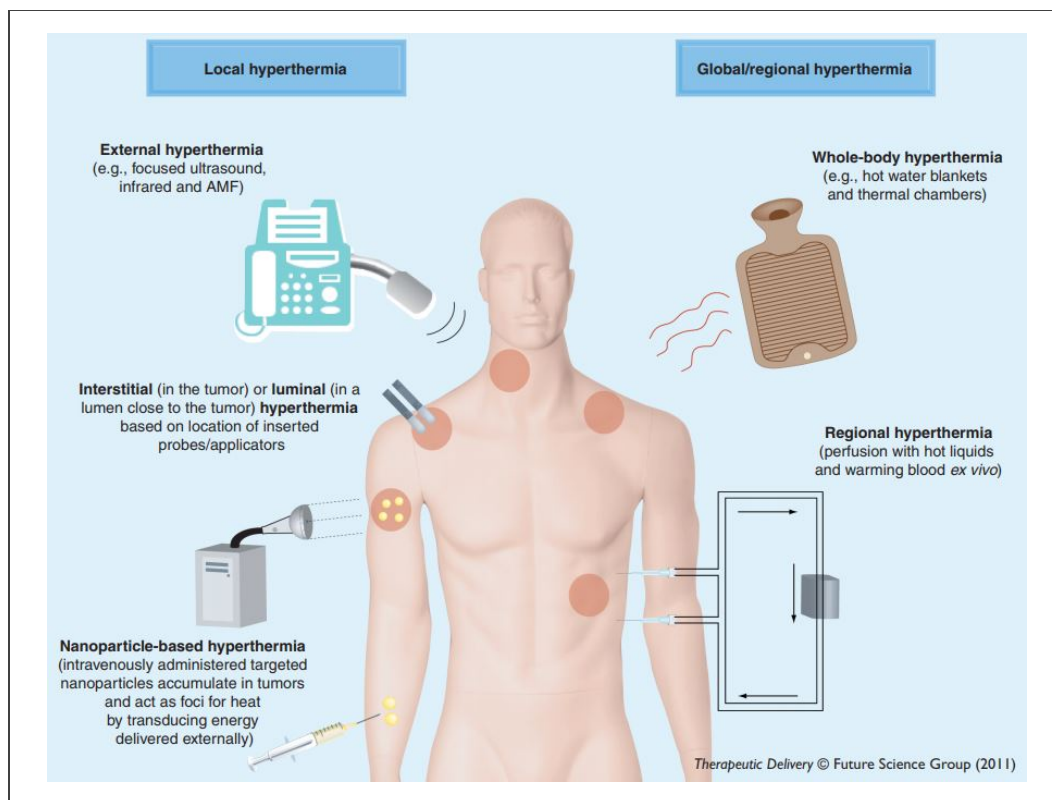


Figure 1.3: Hyperthermia is performed in various ways on patients. It can be divided in local and global hyperthermia; local hyperthermia is made through external sources, with probes, and mediated by NPs. Copied from Ref. 23.

zone affected is larger. For example, regional perfusion is being studied to treat particular cancers located in the limbs such as sarcomas and melanomas. Regional perfusion consists basically in heating the blood of a certain part avoiding the circulation for the rest of the body. The blood is heated outside of the body, then it is pumped back where the cancer is located. The blood can be accompanied with chemotherapy to make more effective the treatment²².

- **Whole-body hyperthermia:** Hyperthermia that can be induced in the whole body for certain cases is being studied. In this treatment the temperature of the body is increased by using heating blankets, thermal chambers, or warm water immersion. The immune system becomes more effective to combat cancer cells in the coming next few hours²⁴.

The most difficult challenge that local hyperthermia must confront is to maintain an exact temperature for a precise range of time. It is difficult to achieve as each tissue of the body responds differently to a certain stimulus. For instance, the brain is very complex and needs specific temperatures. magnetic resonance imaging (MRI) and small thermometers are recommended to monitor the temperature which are improving the hyperthermia treatment. In order to minimize the problems related to hyperthermia, the use of NPs has been implemented. They help to target the tumor, reduces the invasion, and enhances an homogeneous distribution of the heat²³.

Nanoparticles Applied in Hyperthermia Treatments of Cancer

Hyperthermia treatment can affect surrounding healthy cells; during thermal ablation, if the high temperatures is not well monitored, this triggers damages in surrounding healthy cells resulting in undesired side-effects. For this reason, investigations about hyperthermia are being improved in order to heat specifically a targeted zone and provide more effectiveness to the treatment. In order to enhance the efficacy of hyperthermia, researchers have been exploring the input of NPs which can help treating tumors where surgery does not work, such as inside the organs^{23,25}.

During the 1990s, the use of NPs for hyperthermia treatment was being implemented. Academics started to use magnetic fields and NPs conjugated with antibodies, which were administered directly to the malignant tumors. Nowadays, there is a variety of NPs that can be exploited in thermal ablation of cancer. For example, in addition to magnetic NPs heated with an alternating magnetic field (AMF), there are optical NPs heated by lasers, and small bubbles, or silica NPs by US²⁵.

Nanoparticles for hyperthermia treatment were proved in 1957, when Gilchris et al. employed magnetic NPs in lymph nodes. The diameters were in the range of 20 nm to 100 nm and the temperature was raised by 14 °C above body temperature when an external (AMF) was utilized. The working principle of magnetic nanoparticles (MNPs) for hyperthermia treatment is based on the flipping of the magnetic dipoles. When an AMF is applied, the MNPs quickly flip their magnetic polarity. During the flipping process, occurs a hysteretic [or relaxation?] loss that is manifested as heat²³.

Photo induced heating is based on matter-light interaction to increase the temperature. The optical methods to induce hyperthermia by using lasers comprise complications because the light is remarkably attenuated by the tissues making it difficult to obtain good results. These complications are improved by using NPs such as to localize properly the site to be treated. The NPs should be correctly distributed prior to producing an homogeneous temperature in the whole tumor. The NPs absorb the energy from the

light releasing it back under the form of vibrational energy that generates heat. Just certain wavelengths are qualified for optical methods, because the selected wavelength has to be transparent to the tissues and strongly absorbed by the NPs^{21,26}. Gold nanoparticles (GNPs), especially nanoshells and nanorods, are the most popular mediators to induce hyperthermia via optical methods. In particular, GNPs absorb light in the near infrared (NIR) region and transform it to heat by the phenomenon known as surface plasmon resonance (SPR)²³.

Table 1.1: Sonosensitizers employed in sonodynamic therapy with their corresponding conditions and cells treated. Copied from Ref. 27.

Sensitizer	Cell	Frequency (megahertz (MHz))	Time (min)	Animal
5-ALA	C6 glioma	1.0	5.0	rat
ATX-70	DMBA-induced	1.92	15.0	rat
DCPH-P-Na(I)	MKN-45	1.0	10.0	mouse
Photofrin	DMBA-induced	1.92	15.0	rat
PPIX	Hepatoma-22	1.43	3.0	mouse
TiO ₂	C32 melanoma	1.0	2.0	mouse

Ultrasound is frequently used for real time imaging whose contrast is enhanced by the generation of microbubbles. Interestingly, sonosensitizers have been in development due to the high penetrability of US. For example, silicon nanoparticles (SiNPs) were investigated for cancer treatment owing to their US attenuation, which demonstrates the transformation of US to heat through the process called cavitation²⁵. In addition to hyperthermia mediated by US, sonodynamic therapy with the use of sonosensitizers enlisted in Table 1.1 have been investigated as a potential treatment for cancer cells. Cytotoxic effects are triggered in cancer cells when sensitizers attenuate US and cavitation collapses²⁷. However, hyperthermia treatment that comprises US has different complications when the speed of US varies in tissues; however, it can be joined with sonography to produce real time imaging²¹.

The introduction of NPs for hyperthermia treatment is complicated due to several challenges they must confront. In general, the main problem is to generate an homogeneous temperature in the whole body. Actually, NPs take advantage of the vascularization to get the the target; however tumors are poorly vascularized complicating, thus, the travel of NPs to the core of the tumor. Another important issue resides in the production of high quality NPs in the laboratory. The composition and size are the most important parameters that should remain from trial to trial, however it gets more complicated when the NPs become more complex. The last problem is about biocompatibility; NPs must be compatible with the body in order

to avoid side effects prior to, during and after the treatment. For instance, materials such as cobalt exhibits good properties but high toxicity, thus are coated to become biocompatible^{21,23}.

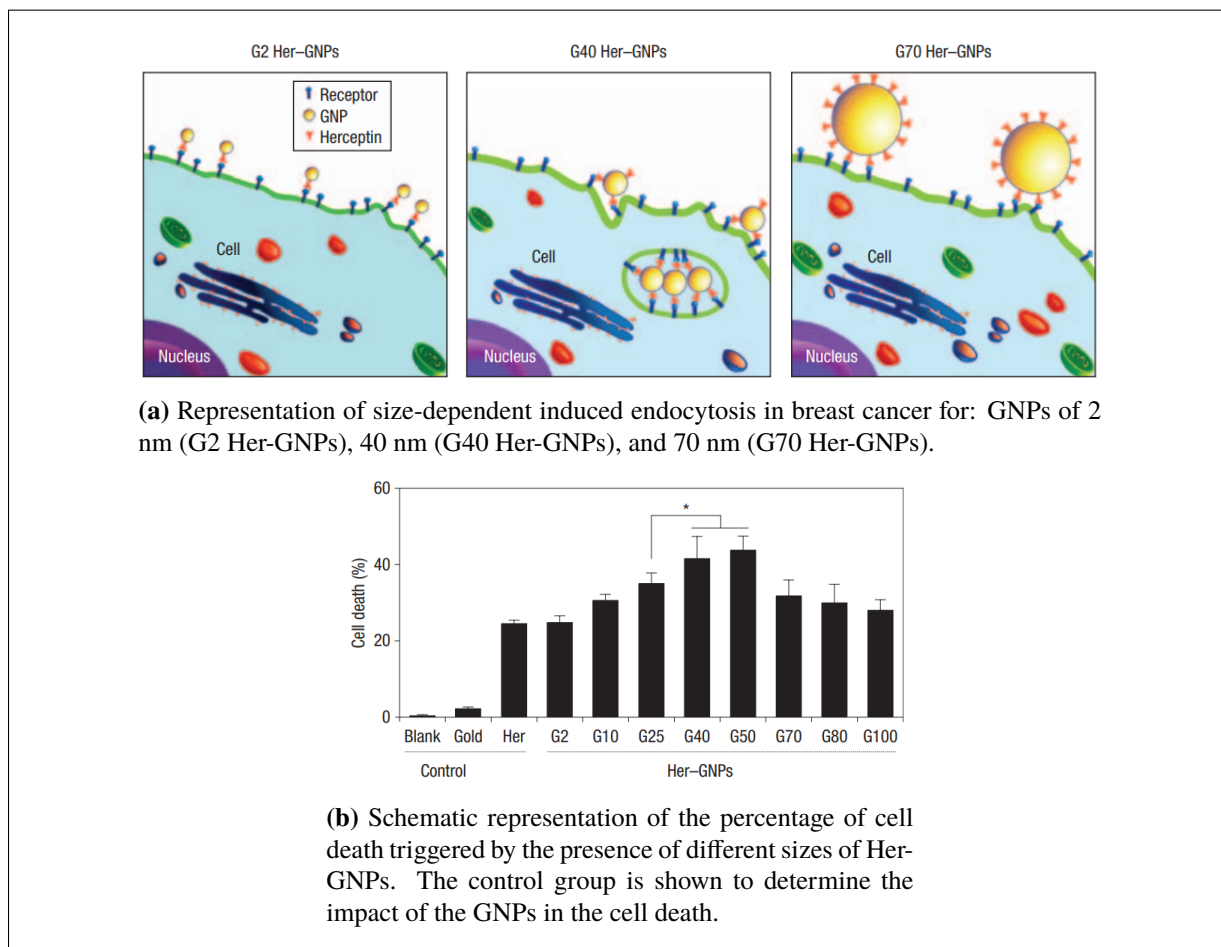


Figure 1.4: Study about the incidence of size in cellular activities through the study of endocytosis and percentage of cell death. GNPs induce endocytosis and can regulate cellular processes of cancer cell resulting in their death. Copied from Ref. 28.

Induced cell death by NPs

Nanoparticles can be internalized within the cells by endocytosis which is clearly demonstrated with Herceptin-Gold nanoparticles (Her-GNPs). GNPs were coated with Herceptin molecules which can link

the receptors tyrosine-protein kinase (ErbB2) present in ovarian and breast cancer. The study of size-dependent during the process of endocytosis revealed that Her-GNPs of a diameter of between 40 nm and 50 nm are the best to produce endocytosis inducing the highest cell death in breast cancer of 45%. In addition, GNPs from 10 nm to 100 nm induced a cell death higher than 30% whose results are shown in Figure 1.4. This experiment showed the good interaction of NPs where they mediated the response of the cell to induce receptor internalization. The results of this study demonstrated that NPs can be used to mediate biological effects, because NPs are capable of regulating cellular processes actively²⁸.

1.1.3 What is PTFE?

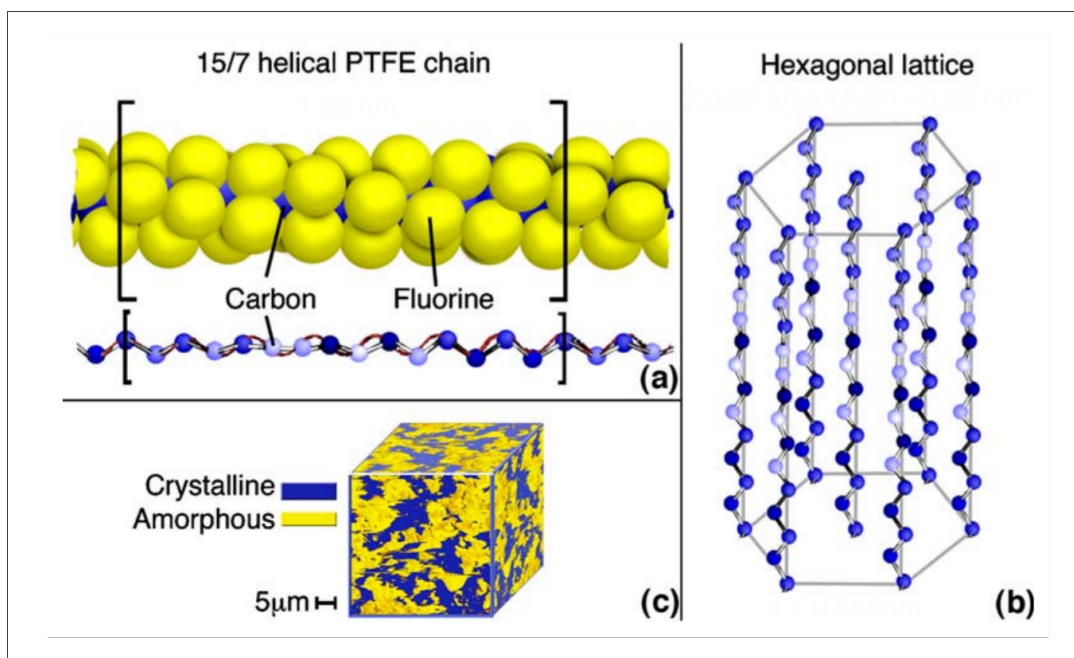


Figure 1.5: Polytetrafluoroethylene conformation of chain and unit cell. **a)**, PTFE is presented in a 15_7 (rotation of 24° and displacement of $15/7 \cdot c$ in z direction) helical chain with a backbone of carbon atoms surrounded by fluorine atoms. **b)**, shows the hexagonal unit cell of PTFE chains. **c)**, PTFE presents an amorphous and a crystalline phase whose percentage is analyzed in the X-ray diffraction (XRD) pattern. At room temperature, PTFE is presented as hexagonal crystal (phase IV), while the amorphous phase is produced by deformations in Phase I (pseudo-hexagonal crystal) and Phase II (triclinic crystal). Copied from Ref. 29.

PTFE or Teflon® is a fluoropolymer made of tetrafluoroethylene (TFE) monomers as shown in Figure 1.5. Fluoropolymers possess fascinating properties and are well-known. In particular, PTFE is chemically inert, with excellent resistance to high temperatures, low dielectric constant, low surface energy, good resistance against weathering; however, it exhibits a high wear rate. This material was discovered accidentally in 1938 by Roy J. Plunkett at the DuPont Company's Jackson Laboratory. At the beginning, it was so expensive to produce and was only employed as a material resistant to corrosion in the Manhattan Project³⁰. Nowadays, PTFE is on the food market with non-stick cookware manufactured thanks to PTFE coatings.

Nowadays, it is also commonly employed in the design of grafts for biomedical applications due to its amazing biocompatibility. Furthermore, fine powder is easily dispersed in water or organic solvents to prepare sealants. Most of the properties stem from the strength of its C-F bonds. It is well known that the bond strength in PTFE are due to the presence of fluorine interacting with carbon. Fluorine has a high electron affinity that tends to attract the electrons to itself in a bond. Additionally, fluorine atoms maintain the carbon backbone integrity which makes difficult to break the chain^{31,32}. The production of PTFE had been patented since its invention. It comprises two steps: first, the production of the TFE monomer followed, then, by its polymerization. This process is detailed in the following sections:

Production of TFE

The first report of TFE production was in 1933. It explains the use of an electric arc to break down tetrafluoromethane followed by the bromination to separate the TFE. Finally, TFE is decontaminated from pyrolysis products using dehalogenation with zinc. This monomer had an enormous success, therefore more ways to produce it were developed. For example, TFE was obtained by the reaction of carbon with carbon tetrafluoride (CF₄) or hexafluoroethane (C₂F₆) at a very high temperatures (1700 °C - 2500 °C). The products of this reaction were quenched and cleaned immediately after the reaction³³.

Other method reports the use of a carbon arc to promote the reaction of elemental fluorine with carbon at 2500 °C - 3500 °C. Other methods were patented in the following years involving the bromination of hydrocarbon gases and their subsequent hydrofluorination with the use of HF to replace the bromine. Another work published the synthesis of TFE through the dechlorination and dimerization of dichlorodifluoromethane. Amalgam of alkali earth metals was employed to enhance the reaction in a medium made of organic solvents³³.

The yield of TFE production increased with other method consisting in the reaction of tri-fluoroethane using hot gases at higher temperatures than 1730 °C, followed by a quick quenching at about 540 °C.

Recent methods presented novel ways of synthesis creating gaseous mixtures with a plasma flame using metal and carbon as precursors. The gaseous reaction is quenched immediately to form TFE. However, the most used method to produce TFE relies on the pyrolysis of chlorodifluoromethane (CHClF_2) when the hydrochloric acid (HCl) molecule is removed. Then, pairs of CF_2 , created by dehydrochlorination, are fused producing TFE³³.

Polymerization of PTFE

The polymerization is indispensable to produce PTFE from the previously manufactured TFE monomers. It can be achieved in several ways such as plasma polymerization. Polymerization was performed in a plasma produced between two disk electrodes. The raw materials used were TFE at 2% of limonene ($\text{C}_{10}\text{H}_{16}$), and a polymerization inhibitor was employed to control the process. The PTFE was deposited in a glass slide, whose rate depends on the power of discharge at the electrodes³⁴.

Furthermore, the process of polymerization can be carried out in aqueous media with heterogeneous processes. Two types can be distinguished: suspension and dispersion polymerization. Polymerization in suspension is characterized by the use of a non-dispersing agent and agitation. The dispersion process for PTFE polymerization uses an aqueous media containing the TFE monomer and ammonium perfluorooctanoate that is agitated in order to obtain a stable colloidal dispersion of PTFE. The dispersion can even be carried out in a carbon dioxide aqueous medium³⁵.

In addition, emulsion polymerization is widely exploited that involves the use of the monomers with initiators and surfactants that start the process of nucleation followed by the growth. This type of polymerization occurs in a reactor with slow stirring cooled by a water flow. The conditions, such as temperature or pressure, do not affect the shape of the PTFE; however, it is important to take care of the concentration and type of surfactants and initiators as they affect the final shape and size³⁶.

Properties

Fluorine is the element with the highest electronegativity in the periodic table. The electronegativity of fluorine is naturally higher than carbon impacting therefore the electron density of the bond. The lone electrons tend to be attracted to fluorine that creates a high electron density around it and a polarization. The size of fluorine atoms does not allow a zig-zag planar crystallization. Instead, a helical zig-zag structure results with fluorine atoms packaged in the spiral backbone of carbons. Twisted zig-zag morphology has a high impact on the properties of PTFE, because it creates a strong and stable C-F bonds. Fluorine atoms

are negatively charged when the polymer is conformed [how? what do you mean?] due to their electron affinity. However, the dipole moment of each C-F bond is cancelled in the conformation of the polymer when the symmetrical structure is manufactured. It leaves PTFE in a neutral electronic state. The most important physical and chemical properties of PTFE are listed in Table 1.2^{37,38}.

Regarding the high chemical resistance, no solvent can dissolve PTFE at room temperature. Just molten alkali and fluorine can affect the surface in certain cases. Additionally, the high viscosity of PTFE is the reason of its thermoplastic properties. This feature is the main reason why PTFE cannot be synthesized by ordinary techniques of polymerization. Commonly, PTFE aqueous radical polymerization is employed to produce PTFE³⁸. Moreover, the high electronegativity of the fluorine atoms creates an extremely hydrophobic surface and its distinguished non-stick properties³⁹. PTFE is transformed under thermally activated phases, thus it adopts helical or planar zig-zag molecular conformation depending solely on the temperature. The distinct structural characteristics in which PTFE is presented are closely related to the rate of wear⁴⁰.

Table 1.2: Summary of the main properties of PTFE. Adapted from Ref. 37,38

Intrinsic properties
Melting point of 327 °C
High chemical resistance
High elongation
High volume or surface resistance
Low coefficient of friction
Low surface energy
Low strength
Low abrasion resistance
Low dielectric constant

Bio-compatibility

The literature reports the biocompatibility of PTFE through different analysis. Cytocompatibility studies demonstrated that PTFE does not induce any cytotoxic effect in contact with endothelial cells, which are present in the interior surface of blood and lymphatic vessels, cells that act as an interface between the blood and the vessel. Cytocompatibility was determined with 2 techniques: MTT assay which is a colorimetric analysis that uses the intensity of absorbance for measuring the growth rate of cells⁴¹; and Neutral Red Uptake (NRU) which uses a dye to determine the cytotoxic activity analyzing the dye recovered

from a cell. In this case, the cytotoxicity is determined in function of the dye concentration, ie, the high concentration of the dye the less cytotoxic effect⁴².

Hemocompatibility tests were executed demonstrating the good affinity of PTFE to human blood. The study, made at 37 °C for 1 hour, showed that Teflon® does not induce hemolysis which is the destruction of red blood cells suggesting its excellent affinity to the blood³¹.

Immunogenicity analysis was tested to determine the host response. For instance, lymphocyte proliferation tests are useful to determine the immune response. There are two types of lymphocytes: T and B that are in charge of conducting different immune functions. Lymphocytes, situated or purified in the spleen, are part of splenocytes which are one of all the white blood cell lines⁴³. The test demonstrated the absence of lymphocytes proliferation with PTFE, this emphasizes the non-immunogenicity nature of this material. Additionally, another study of immunogenicity with macrophages was made. Macrophages are a line of white blood cells in charge of managing the immune system which are formed in response to infections and antigens. These are important mediators of biocompatibility. This is why they are used to determine the immunogenicity. Finally, the study reveals a non-inflammatory and non-activating nature when PTFE is present in macrophage cultures³¹.

Applications

It is known that PTFE is hydrophobic, whose analysis of water-contact angle gave about 108°. Moreover, PTFE in combination with other materials, it is capable to generate superhydrophobic and superoleophilic surfaces. Intrinsic properties, such as the crystal structure, or in combination with carbon nanotubes or microporous paper can affect its behavior with water. Superhydrophobic and superoleophilic materials are widely used by oil companies to purify the oil⁴⁴⁻⁴⁶.

Teflon has been potentially used in the medical field, it was applied as an artificial heart valve. Currently, it is expanded by creating micropores on the surface [of what?] and is used for bypass grafting which is a type of surgery that betters the blood flow in the heart. The expanded PTFE prevents atherosclerosis which is a blockage in the arteries. To summarize, PTFE is the best alternative as a bypass material.^{47,48}. Another special application was made with PTFE-coated platinum-iridium wires which were inserted in the vitreous cavity of three albino rabbits during six months to determine its biocompatibility. At the end of the test, the coatings were intact which means that the integrity of the Teflon was preserved indicating its excellent biocompatibility⁴⁹. Furthermore, PTFE grafts can help in drug delivery acting as conduits to deliver the drug to the exact place⁵⁰.

More studies demonstrated that pressed PTFE powder has good reflection properties in the visible region. Results determined that this material has an enormous capacity for being employed in reflectance spectrophotometry and other signal-averaging devices⁵¹. From homes, companies and hospital, PTFE is recognized due to its amazing properties. In the daily life, Teflon[®] is present in electric wire coating, small and large diameter tubes, sealing tapes, spray lubricant, gaskets, non-stick cookware, among others.^{32,52}.

1.1.4 Ultrasound in Medicine

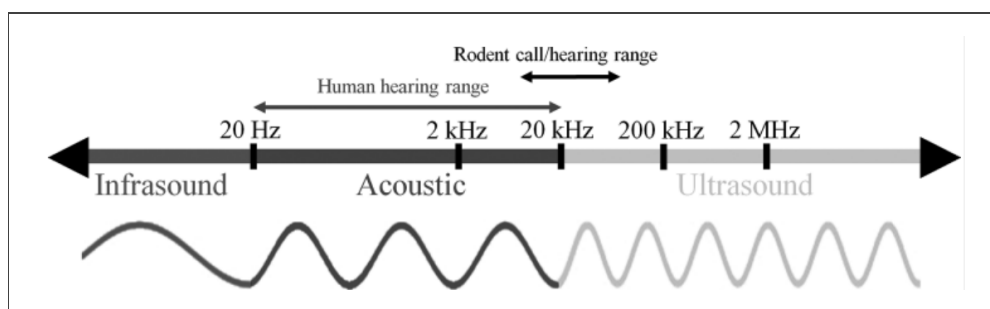


Figure 1.6: Illustrative sketch of sound frequencies, which are useful to differentiate the sound in different ranges for different applications. Copied from Ref. 53.

Ultrasounds (US) are located in the range where the human ear can not hear. The frequency of US is above 20 kilohertz (KHz) as shown in Figure 1.6. Ultrasound is widely employed in medicine, especially for imaging where high frequency sound waves travel through the body whose echo is monitored to make the image. Frequencies in the range of 2 - 10 MHz are used in imaging, whose speed of propagation through the body depends on the density of the tissues. The penetration of the waves depends on the frequency employed. For example, deeper tissues are reached with low frequencies whereas tissues near the body surface are reached with high frequencies⁵⁴.

Several therapies have been carried out with the use of US. For instance, high intensity US is used for tissue heating while low intensity does not increase the temperature. The low intensity US is used in a enormous variety of medical applications, such as bone healing, soft-tissue regeneration, inflammation inhibition, neuromodulation, dental treatment, among others. The results obtained with US application are admirable. For instance, US helps to reduce the fracture healing time, promotes tendon healing, among others⁵⁵.

1.1.5 The Behavior of Teflon® Under Ultrasound

The expanded polytetrafluoroethylene (ePTFE) is a porous material of nodes and fibrils that creates a network comprising more than 70% of the volume of common PTFE. The ePTFE maintains all the positive chemistry features than PTFE, and also with improved mechanical properties⁵⁶. ePTFE is frequently used in vascular grafts but causes, sometimes, hyperplasia leading to the graft failure. This problem is solved by using high frequency ultrasound in order to rise up the temperature of the graft to prevent hyperplasia⁵⁷.

A study about modelling ePTFE as vascular grafts on soft tissues and blood demonstrated the ultrasound attenuation of the graft. Ultrasound sources of 1.5 and 3.2 MHz were simulated in two graft-tissue models: one with and the other without hyperplasia. The results determined that ePTFE exhibited higher attenuation to ultrasound at both frequencies. Whereas the transducers increase significantly the blood temperatures, the hyperplasia affects only the temperature of the nearby soft tissues. The temperature of the vascular graft with hyperplasia showed approximately 50 °C after 30 seconds of ultrasound exposure using both transducers: an acoustic power of 0.6 watt (W) for the transducer of 1.5 MHz and 0.375 W for the one of 3.2 MHz. It is well known that cell death occurs at about 50 °C, thus the grafts can prevent hyperplasia under the effect of ultrasound. Additionally, it does not matter where the ePTFE graft is located, because the low frequency ultrasound (1.5 MHz) is appropriate to produce hyperthermia in sites deeper in the body while the high frequency ultrasound (3.2 MHz) is recommendable for external sites located near the body surface. To sum up, the literature reports the high attenuation of ePTFE grafts which is 10 times greater than that of the surrounding tissues that subsequently increase the temperature of the graft at about 50 °C, a temperature high enough to induce apoptosis⁵⁷.

Another work of a thesis study in the University of Utah was based on the analysis of PTFE tubes under the effect of the ultrasound at different frequencies. The attenuation demonstrated by the PTFE tube is shown in Figure 1.7. The experiment was carried out in a liquid medium using water at an initial temperature of 37 °C to simulate blood and a PTFE tube as a vascular graft. The experiment was performed in two ways: one with water flow along the PTFE tube and the other without water flow. The transducer was placed perpendicular at 15.2 cm away from the surface of the tube placing the focal point 1.1 cm past the tube back wall. It is recommendable to move the tube closer to the transducer, because the beam has a larger diameter, and thus it is easy to locate the thermocouples in order to obtain the data of the temperature. Final results demonstrated the ultrasound attenuation of the PTFE tube under a frequency of 1.5 MHz where the temperature reached almost 49 °C in the back wall while in the test with water flow the temperature increased up to 46 °C. The focal point should be placed exactly in the wall on the PTFE tube as the power is most concentrated in that point producing the higher temperatures. Comparing the

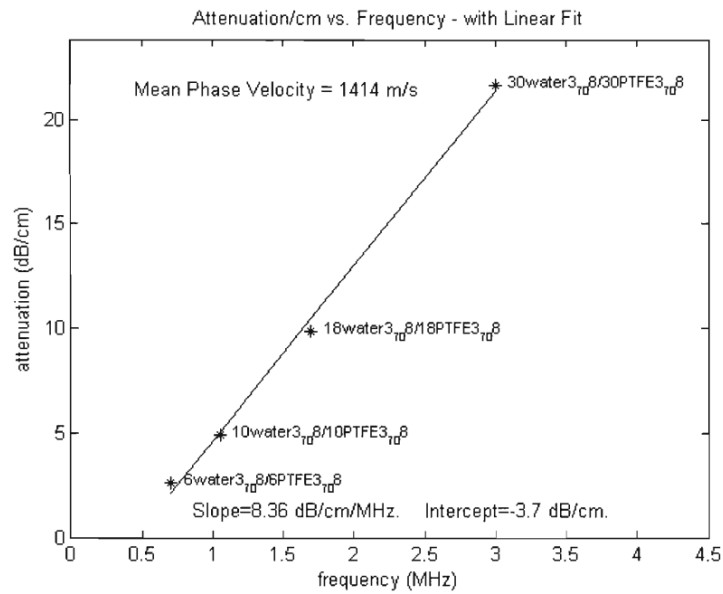


Figure 1.7: Attenuation of ultrasound by a PTFE tube of 4.75 mm of thick. The asterisks represents the four frequencies at which the tube was subjected, starting from 0.7 MHz to 3 MHz. Copied from Ref. 58.

attenuation of ePTFE and PTFE was determined that ePTFE has less attenuation of ultrasound due to the pores [what?]⁵⁸.

1.2 Problem Statement

Cancer is commanding the mortality rate around the world. This rate is even higher in developing countries, including the Latin American regions. In fact, the incidence of cancer in Ecuador is worrying; a study of WHO revealed that about 1 out of 6 deaths are the outcome of cancer, which is associated with oil activity, concomitant migration, crowding, and poverty. Among the frequent treatments offered by public health centers in Ecuador, one can cite: surgery, radiotherapy, chemotherapy, targeted cancer therapy, and stem cell transplant. Importantly, new improvements have been introduced, during the last decade, to improve the efficiency of frequent treatments. Metallic, polymeric, among others NPs are under study to be applied in the medical field. Nowadays, it is possible to observe great advances in the use of magnetic NPs heating with external magnetic fields, optical NPs heated by lasers, small bubbles with US, and NPs that induce cell death by endocytosis. The main obstacles of the new emerging treatments with the use of NPs are: biocompatibility, immune response, real-time monitoring, cost needed, and efficacy. Most of the troubles are solved by choosing the adequate material and optimizing the protocols. NP-mediated hyperthermia is one of most explored treatment for cancer ablation, this relies on the use of external sources of energy, such as US, AMF or electromagnetic radiation. The external sources affronts difficulties when are directed to the body due to its complexity. On one hand, AMF is considered to be the best way to implement hyperthermia but it utilizes metallic NPs that can cause post-treatment side-effects because it is difficult to track them in the body which may ultimately trigger an immune response due to their poor biocompatibility. Furthermore, patients with metallic grafts can not be treated this way as the applied magnetic field can give rise to complications. On the other hand, it is possible to rely on optical methods to carry out the hyperthermia; however, it comprises complications as the light is attenuated and reflected by the biological tissues. Finally, NPs heated via US attenuation present problems as the speed of US varies in different tissues. Regarding the problems with US, it is possible to provide several advantages that make a novel way to induce hyperthermia. For example, it is possible to employ different frequencies to reach places deeper in the body or locations near to the body surface. Moreover, US-induced hyperthermia can be monitored in real time by using sonography. With respect to the type of material, it is crucial to select a material that does not produce cytotoxic effects, hemolysis, nor any immune response. For these reasons, PTFE has been chose to be employed for US attenuation owing to its outstanding properties. PTFE has been used in the medical field for grafts, implants, drug delivery, among others. Additionally, the response of PTFE under US exposure has been investigated with simulations and experimentally. Results show that bulk PTFE attenuates the US from 1 MHz to 3 MHz generating temperatures up to 50 °C. This temperature can be modulated to fall in the optimal range of hyperthermia (41 °C - 45 °C), by tuning the external parameters,

such as time of exposure, focal point or frequency. Finally, literature reports the optimal diameter of NPs is circa 40 nm to be internalized via endocytosis and induce death of cancer cells.

1.3 General and Specific Objectives

General objective:

The aim of the present project is the production of polymeric NPs made of PTFE starting from sealants, characterize them using several techniques (UV-Vis, XRD, TEM, FTIR) and carried out the preliminary studies regarding their behavior when subjected to US and X-ray imaging.

Specific objectives:

- To review ancient and modern causes of cancer in Ecuador with the treatments that are being offered by public health centers.
- To expose the advantages, working principle, and advances of different hyperthermia methodologies.
- To exhibit the fascinating properties of Teflon® that can be potentially applied in the medical field.
- To analyze the ultrasound attenuation demonstrated by PTFE which is not well known in the scientific community.
- To open new venues for the exploitation of ultrasound in the medical field and discuss their main advantages.
- To follow the trial and error method in order to synthesize PTFE NPs.
- To characterize the as-fabricated PTFE NPs via different spectroscopies and techniques of characterization acquired during my undergraduate studies.

Chapter 2

Methodology

This chapter of methodology provides more detailed discussions and derivations of the theoretical basis and methods employed within the present work. This material is taken from literature and is presented in summary form to best elucidate the context of results and analysis provided in Chapter 3. The methodology used for the development of this thesis can be divide into 2 sections in order the provide accurate information making everything reproducible.

- **Synthesis of polytetrafluoroethylene (PTFE) fine-powder and nanoparticles (NPs).** This section contains information about the synthesis of PTFE NPs. The synthesis also was divided into 2 subsections in order to detail the production of PTFE fine powder and, using this fine powder, the preparation of a stable colloidal solution of PTFE NPs.
- **Characterization.** This section explains the types of characterizations to which the PTFE fine-powder and NPs were subjected. Various types of characterizations were performed which were selected according to the material under analysis. Therefore, each subsection details what material was characterized either powder or NPs.

2.1 Synthesis of PTFE Fine-powder and NPs

PTFE NPs were produced from a fine-powder, thus prior to the production of NPs the synthesis of the fine-powder is explained. The fine-powder was obtained from a commercial sealant by using the trial and error process. The reagents employed and protocol created for the powder production are itemized in the

Chapter 3, subsection 3.1.1.

The PTFE NPs were prepared in colloidal suspension, thus two methods were employed. Sonication was used to disperse agglomerates of PTFE fine-powder within the liquid phase, while differential centrifugation was employed to separate the NPs per size. To continue, both techniques are explained in detail:

2.1.1 Sonication

Sonication is the use of ultrasonic power to obtain a full dispersion of dry powder in a solvent. Through this way, it is possible to break down agglomerated particles to obtain smaller ones due to powder fragmentation. Usually, sonication uses inaudible frequencies, higher than 20 kHz that the human ear can not hear. Sonication can be performed with pulses or can be constant. Additionally, it is considered a simple tool to obtain very small NPs, thus it is relatively inexpensive. As a consequence, this method is widely employed by toxicological and environmental studies to powder fragmentation or re-disperse stock suspensions. The application of non-standardized sonication protocols can influence the final result producing complex physical and chemical phenomena. For a better explanation, the concept of NPs is presented. NPs are ultra-small particles characterized by at least one dimension between 1 nm - 100 nm. Additional information about primary particle or nucleus is explained. Primary particles are the smallest one within a group of particles which may form larger particles by agglomeration. There are two types of larger particles structures: aggregates and agglomerates. An aggregate is a junction of several primary particles whose bonds are difficult to break which can be fused, sintered or display a metallic bond. On the other hand, an agglomerate is the joining of smaller particles but with the distinction of weak bonds such as van der Waals (vdW), capillary or electrostatic interactions. For this reason, agglomerates can be broken down by using sonication in order to obtain primary particles. The separation of agglomerates in a solvent creates a colloidal solution which is a liquid dispersion where small particles are homogeneously distributed⁵⁹.

The process of sonication is generated by sound waves propagating through the liquid medium in alternating high and low pressure cycles. Commonly, the frequency of sonication is between 20 - 40 kilohertz (KHz). During the low pressure cycle, known as rarefaction, vapor bubbles of some micrometers are created due to the cavitation process. The bubbles created are broken during the high pressure cycle (compression) that produces a local shock wave which releases an enormous amount of mechanical and thermal energy. The schematic representation of the effects produced by high and low pressures are shown

in Figure 2.1. There are different ways with which ultrasonic waves are produced. With a probe which is directly inserted in the liquid medium, or introducing the sample in a bath where the ultrasound (US) waves are propagating as shown in Figure 2.1.

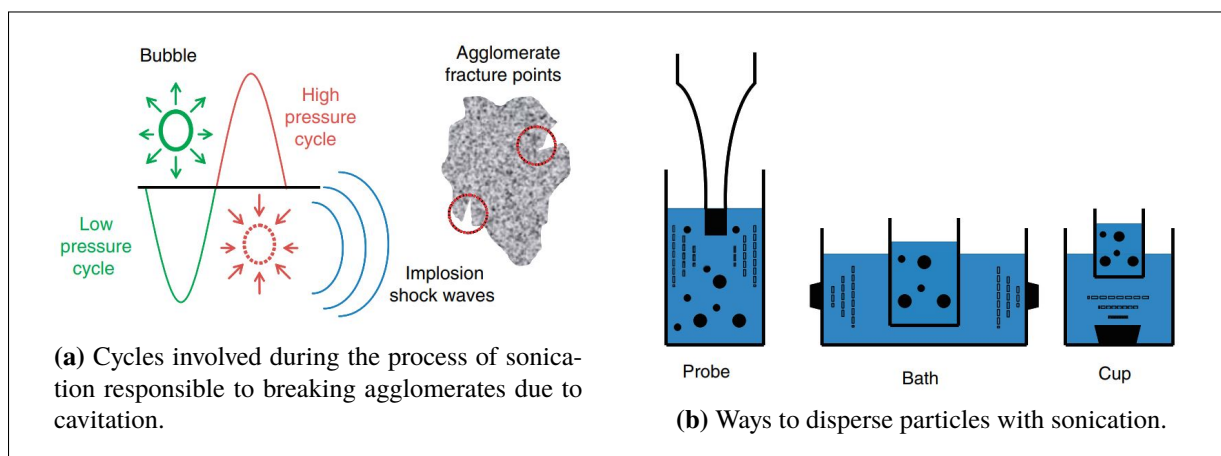


Figure 2.1: Graphical description of: (a) the process of cavitation produced into the liquid phase due to waves of ultrasound, and (b) ways to carry out the sonication of the samples. Copied from Ref. 59.

The output local energy is responsible to breaking down the agglomerates into primary particles. The ultrasonic device creates vibrational energy from electrical power with the use of a piezoelectric. The piezoelectric responds with a physical change of volume when an AC current is applied. The power delivered during the sonication is specified by the manual guide. However, some systems are capable of detecting when the vibrational frequency of the transducer experiment has a high resistance. The oscillation frequency is usually fixed by the instrument. Amplitude and power can be tuned to increase the amplitude of the oscillations making more effective the process of break down agglomerates of higher resistance. The best way to optimize the dispersion process is with the trial and error approach because the guidelines offered are based on a strict protocol which can be used to tune new parameters⁵⁹.

2.1.2 Differential Centrifugation to Separate NPs per Size

Size and shape of NPs are essential features for any intended applications, such as drug delivery where homogeneous [in what sense? size or colloidal stability?] solutions are needed. Effects, such as a longer circulation in the blood stream or interaction with the cells, are impacted by the size and shape, respectively.

During the synthesis of NPs, a homogeneous result is challenging where complex thermodynamics and kinetics are introduced to optimize their production. In order to solve the problem of heterogeneous content of a population of NPs, different methods have been developed such as: size exclusion chromatography where hard and soft NPs are separated by size; purification by centrifugation relies on the centrifugal force to separate the NPs per density. The revolutions per minute (RPM) or relative centrifugal force (RCF) depends directly on the density of the NPs and medium. This process involves some basic steps which can be optimized. In the first step, a solution is centrifuged at a low RCF or RPM for about 20 minutes. Then, the supernatant is removed and centrifuged at higher RCF for the same time (20 minutes) as shown in Figure 2.2. This step is repeated but increasing the velocity. For instance, it is possible to start with 5,000, then 10,000, 15,000 and 20,000 RCF⁶⁰.

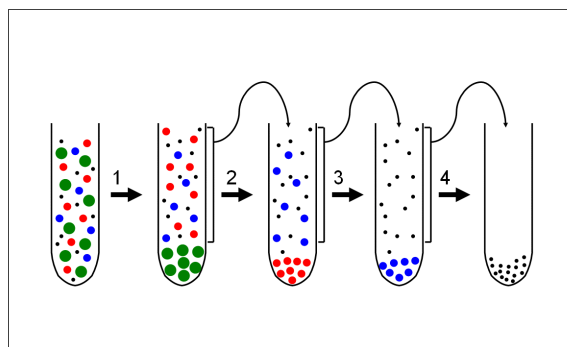


Figure 2.2: Process of Differential Centrifugation to obtain smaller particles. It involves a continuous process where the supernatant always contains the smaller NPs. Copied from Ref. 61.

The device used to produce the centrifugal force is known as centrifuge. It is driven by a motor to reach high speeds. During the process of centrifugation, the particles suspended tend to move radially outwards toward the inside of the centrifuge tube creating a precipitate (pellet). The fluid that remains in the upper part of the sample is known as the supernatant. The Stokes equation 2.1 can be applied to calculate the necessary time for sedimentation of particles bigger than a specific size⁶².

$$T = \frac{9l\eta}{2r^2(\rho_p - \rho_s)\omega^2 R} , \quad (2.1)$$

where,

- T , Necessary time to precipitate particles (s).
- ω , Angular velocity ($rad \cdot s^{-1}$).
- r , Radius of suspended particles (m).
- η , Viscosity of the solution ($Pa \cdot s$).
- ρ_p , Density of suspended particles ($Kg \cdot m^{-3}$).
- ρ_s , Density of solution ($Kg \cdot m^{-3}$).
- R , Radius of the circular motion of the centrifuge (m).

The earth gravity is not considered because the force created during the centrifugation is thousands of times bigger. The equation is useful to determine exact times; however, it is difficult to fulfill all the parameters needed. For that reason, the trial and error learning is considered better to optimize the process of differential centrifugation. The density and viscosity of some substances is not well known in most of the cases producing non-realistic results⁶².

2.2 Characterization of PTFE

2.2.1 Diffuse Reflectance Ultraviolet Visible (UV-Vis) Spectroscopy

This technique is based on the same principles of common UV-Vis. It is associated with the excitation of atoms from basal to higher energies. It is well known that transitions are obtained with precise energies. An excitation occurs when an electron is excited from the ground state to an excited state. The light presents different energies at different wavelengths. The particular energy delivered is capable to induce just one electronic transition. Energy and wavelength are related in the equation 2.2, where the Planck constant is introduced⁶³.

$$E = \frac{hc}{\lambda} , \quad (2.2)$$

where,

- E , The photon energy.
- h , The Planck constant.
- c , The speed of light.
- λ , Photon wavelength.

Therefore, when the gap between energy levels is larger, the energy necessary should be higher (short wavelength). UV-Visible spectroscopy employs this concept to generate the spectrum. In the devices, the absorbance is measured usually in the range between 200 to 800 nm. The light source produces a beam focused to a prism in order to create light beams of different wavelengths in the range of 200-800 nm. The light of different energies travels through the sample which is placed in a transparent cuvette. Then, the detectors are in charge of measuring the output light coming from the sample. Detectors transform the light into a current with which it is possible to create a plot where higher currents means high intensities. A blank is always employed which is useful to eliminate the absorbance produced by the solvent in which the important particles are suspended. The absorbance is calculated with the equation 2.3⁶³.

$$A = \log_{10} \frac{I_o}{I} , \quad (2.3)$$

The absorbance is calculated for each wavelength, where I_o is the intensity of the incident light and I is the intensity of transmitted light. The absorbance presented in the plots is proportional to the concentration according to the Beer-Lambert Law. Therefore, it is possible to determine the concentration of a solution by plotting a calibration graph. The Beer-Lambert law establishes the relationship between the absorbance and the concentration of a colloidal dispersion, as shown in equation 2.4⁶³.

$$A = \varepsilon \cdot C \cdot l , \quad (2.4)$$

where,

- A , Absorbance
- ε , Molar extinction, this value is particular for each substance at a certain wavelength ($dm^3 \cdot mol^{-1} cm^{-1}$).
- C , Concentration of the solution ($mol \cdot dm^{-3}$).
- l , Dimension of the cuvette (cm).

Diffuse Reflectance Spectroscopy

In addition to the conventional spectrometry where liquid samples are measured, diffuse reflectance spectroscopy is widely exploited to analyze powders with minimum sample preparation. The reflectance spectrum is obtained from the reflected light coming from a uniform surface of the powder. There are two types of reflection that can occur: regular or specular, and diffuse that are presented in Figure 2.3. Regular reflectance appears usually by employing polished surfaces, like mirrors, while diffuse reflection arises with the reflection of light over a dull surfaces, like powder. Reflectance spectrum can be tricky at

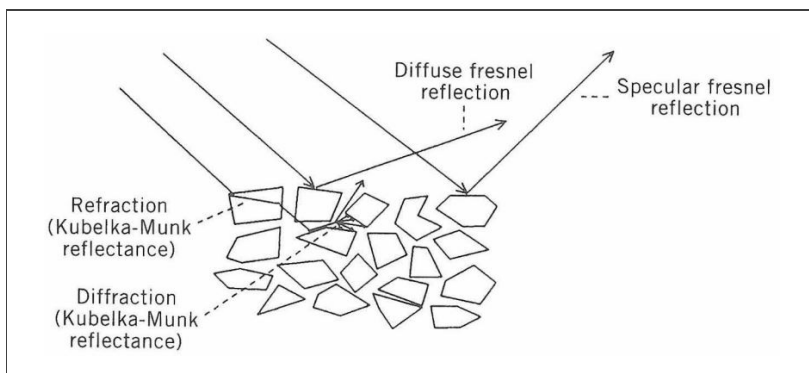


Figure 2.3: Optical phenomena produced during diffuse reflectance in powder samples. Copied from Ref. 64.

the analysis moment, therefore there are some methods to transform it to the well known absorbance⁶⁴.

Various authors use the famous equation 2.5 that relates directly the absorbance (A) and reflectance (R). However, that approximation does not consider the scattering processes, such as refraction or diffraction (Figure 2.5) that are induced inside the sample due to inhomogenities⁶⁴.

$$A = \log_{10} \frac{1}{R}, \quad (2.5)$$

In order to solve this problem, the Kubelka Munk (K-M) model has been developed to give a simple solution for semi-infinite samples. The equation 2.6 embraces the whole scattering processes with a simple constant s where the k is the absorption coefficient of the sample and R is the diffuse reflectance⁶⁵.

$$R = 1 + \frac{k}{s} - \sqrt{\frac{k}{s} \left(2 + \frac{k}{s} \right)}, \quad (2.6)$$

The K-M equation is solved in a simple way where the absorbance is almost equal to k as shown in equation 2.7. The s (scattering coefficient) describes the particle size and refractive index of all the particles in the sample. This coefficient does not suffer notable changes with different wavelengths. However, s is highly influenced by the packing density, it means that the way in which the powder is prepared for the analysis should be maintained⁶⁵.

$$A \approx \frac{k}{s} = \frac{(1 - R)^2}{2R}. \quad (2.7)$$

2.2.2 X-ray Powder Diffraction

It is a non-destructive and analytical technique that provides information about the phase of crystalline materials, chemical composition and physical properties. For example, in order to know the average bulk composition of a sample, a small amount is ground and analyzed. Lattice parameters, crystalline sizes or preferential orientation can be studied through this technique. In 1912, Max Von Laue discovered that crystals are conformed by ordered structures as they can produce diffraction when X-rays are directed to the crystals. Atoms ordered in a periodic lattice produce elastic scattering of monochromatic X-rays. X-rays diffracted obey the Bragg's law, shown in Equation 3.4, giving constructive or destructive interference depending on the phase in which the waves are founded. The schematic of this process is shown in Figure 2.4⁶⁶.

$$n\lambda = 2d\sin\theta \quad , \quad (2.8)$$

where,

- n , Integer number known as order of reflection.
- λ , Wavelength of the X-rays.
- d , distance between crystal planes.
- θ , angle formed between the incident X-ray and the normal of the crystal plane.

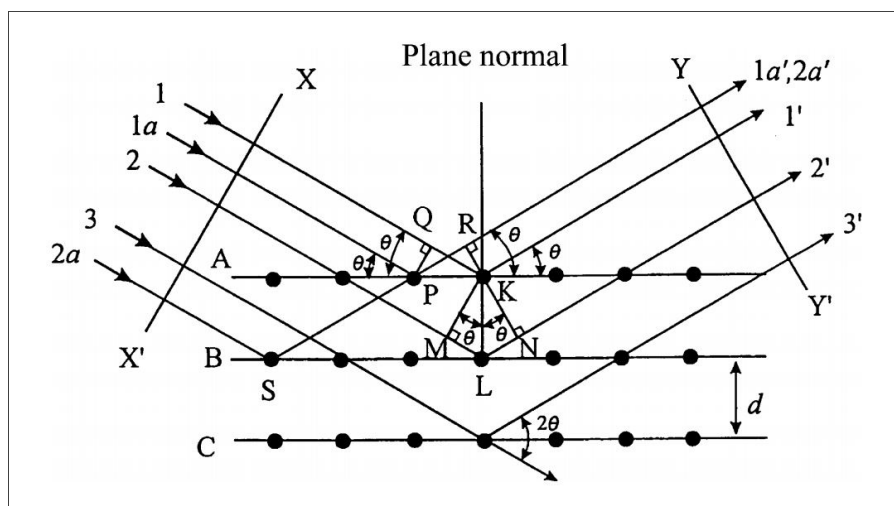


Figure 2.4: Schematic representation of X-ray diffraction (XRD) and Bragg's law. Copied from Ref. 66.

Bragg's equation is useful to determine the distance between planes of a crystalline structure. Moreover, it is possible to determine the angles that produces constructive and destructive waves. The diffraction pattern is effective to determine an unknown substance, because the peaks created can be compared with huge databases that collects information of intensities and positions of various compounds. The diffraction pattern is useful to determine the phases of a crystal, only the presence of intense peaks ensures the existence of a crystal structure. In some case, multiphases are determined by comparing the smallest characteristic peaks. The peak angles are essential to determine lattice constant, stress, particle size, and degree of crystallization. Instrumentation to produce X-ray pattern consists of three basic elements: X-ray tube, sample holder, and X-ray detector. X-rays are generated inside the tube when electrons are accelerated under high voltages toward a target. When electrons hit the target, this produces the excitation of electrons that are in the atoms of the target. The excited electrons release energy when they go back to the ground state. The energy released by the recombination is enormous which is transformed in electromagnetic radiation of short wavelength known as X-rays. Copper is the most common material employed as target to produce X-rays. The X-rays are collimated and directed towards the sample. The reflected X-rays are monitored constantly while the sample and detector rotation. The detector records and processes the incoming signal to finally produce the pattern^{67,68}.

2.2.3 X-ray Imaging

X-rays are a type of high energy electromagnetic radiation. These rays are created by the collision of electrons that are moving with high kinetic energy. Usually, electrons are created in the cathode due to thermoionic radiation and are accelerated towards the anode due to the attraction of electric charges. The collision between electrons and the anode generates high energy radiation (X-rays). It is possible to control the amount and the energy of produced x-rays. For example, the tube current (mA) tunes the amount of electrons produced, which is directly proportional of the number of X-rays while the tube potential (kV) modulates the electron energy that controls the x-ray energy. In summary, the tube current (mA) controls the amount of X-rays while the tube potential (kV) controls the energy of X-rays⁶⁹.

X-ray imaging systems are assembled to detect high energy radiation by using semiconductors as detectors. The detectors must sense the electrical charge pulses that are created when the material absorbs the X-rays. The detection of the charge pulses are essential to produce the image which determines the resolution; however, more information is required for imaging. X-ray imaging is applied in a variety of fields for security, material science and inspection, medical imaging, or particle physics research. X-rays travel through the sample and are detected, giving rise to the transmission image. The contrast is produced

by the energy of the detected phonons. The absorption of the sample decreases with increasing tube potential (X-rays energy) that results in a lost of contrast. Therefore, it is important to manage the tube current and potential to obtain better images⁷⁰.

2.2.4 Ultrasound Imaging

Medical imaging have advanced and different ways to analyze the body have been devised, such as X-ray radiography, X-ray computerized tomography (CT), ultrasound, nuclear imaging, magnetic resonance imaging (MRI), and optical imaging. However, ultrasound imaging is contemplated as the most cost-effective. US imaging is safe and produces real time imaging, good for obstetrics and cardiology. Nowadays, US is the second most used diagnostic imaging in medicine just after X-rays. This technique possess advantages over the conventional techniques. For example in Table 2.1 are enlisted advantages and disadvantages⁷¹:

Table 2.1: Advantages and disadvantages of US imaging in comparison to other modalities, such as X-ray computed tomography (CT), radionuclide emission tomography, and magnetic resonance imaging (MRI). Adapted from Ref. 71.

Advantages	Disadvantages
<ul style="list-style-type: none"> · Ultrasound is a form of nonionizing radiation and is considered safe to the best of present knowledge. · It is less expensive than imaging modalities of similar capabilities. · It produces images in real time, unattainable at the present time by any other methods. · It has a resolution in the millimeter range for the frequencies being clinically used today, which may be improved if the frequency is increased. · It can yield blood flow information by applying the Doppler principle. · It is portable and thus can be easily transported to the bedside of a patient. 	<ul style="list-style-type: none"> · Organs containing gases and bony structures cannot be adequately imaged without introducing specialized procedures. · Only a limited window is available for ultrasonic examination of certain organs, such as heart and neonatal brain. · It depends on operator skills. · It is sometimes impossible to obtain good images from certain types of patients, including obese patients.

Despite the fact that US imaging presents drawbacks, its advantages are good enough to determine it

like a valuable tool in the medical field.

When US travels through the body, its initial energy is reduced or attenuated as a function of the distance. The attenuation of US is used to produce contrast in the images. For the analysis of blood flow, the Doppler effect is considered by using the data collected from red cells. Transducers are in charge to produce gray-scale ultrasonic imaging, because they produce and receive the signals⁷¹.

To enhance the images, contrast agents have been employed. During the 1990s, the production of microbubbles was standardized to study the effect of ultrasound. Commonly, the agents are microbubbles that contain air or high molecular gases encapsulated by lipids. The bubbles are small enough (1 - 10 μm) to travel through the blood and pass the capillaries. When the diameter of the bubble is 1000 smaller than the wavelength of the US, they resonate as a response of US that is 20,000 times greater than water; the resonance increases while the diameter of bubbles increases. However, the microbubbles can be destroyed by several factors, such as high intensities, ultrasonically enhanced diffusion and the absence of ultrasound⁷².

2.2.5 Transmission Electron Microscopy

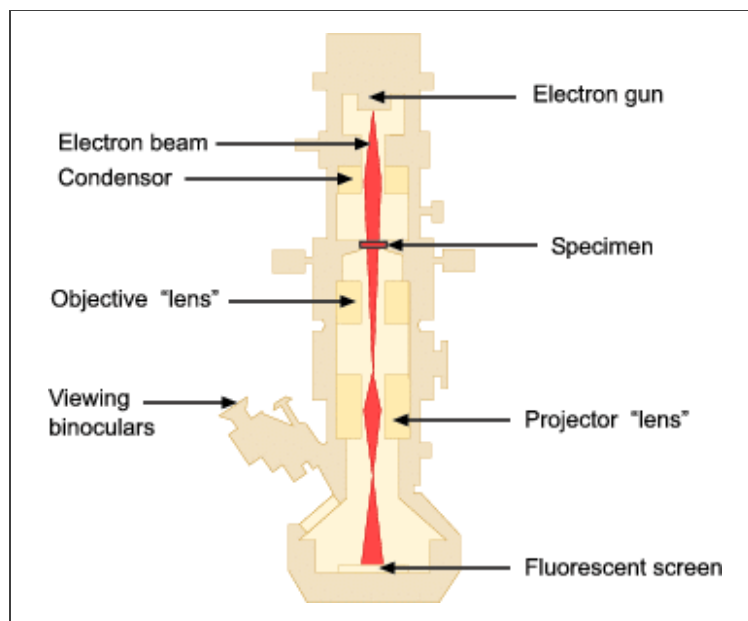


Figure 2.5: Schematic representation of a Transmission Electron Microscopy (TEM). The image represents the way in which the electron beam is created and the image produced. Copied from Ref. 73.

Indeed, TEM is exploited in nanotechnology and related areas. Electrons are responsible of producing images, diffraction patterns and chemical analysis, because they behave as waves and as particles. The wavelength of electrons is so small that it can interact even with atoms of a sample. It is indispensable to know the electron scattering principle that is the base of image production. Firstly, electrons are accelerated by using high power in the filament. Then, magnetic lenses produce magnetic fields to align the electron beam. It is important to set a high vacuum inside the chamber to avoid collisions between electrons with gas atoms and prevent electrical arcing. The electron beams are focused toward the sample holder containing the specimen. The imaging system has electromagnetic lens to refocus the output beam from the sample. An additional lens enlarges the image to be projected on the screen. The screen is capable of detecting the incoming electrons with a phosphorescent plate that glows when hit by electrons. Usually, the samples should be ultra-thin or colloidal suspension^{73,74}.

The electron beam is produced in a tungsten filament which is connected to a high voltage in the range of 100-300 kV. The production of electrons is explained either by thermoionic or field electron emission. The beam created in the filament is instantaneously accelerated by several electrostatic plates; once the optimal velocity is reached, it enters to the next part of the microscope. Electromagnets are employed to focus the beam by using magnetic fields. Additional lenses magnify the beam that leaves the sample from 100 to more than 1,000,000 times. Basically, TEM consists of three sets of lenses. There are condenser, objective, and projector lenses as shown in Figure 2.5. Condenser lenses are near the beam source correcting and focusing it. Objective lenses focus the beam toward the sample. Finally, projector lenses are placed after the sample to magnify and correct the beam which traveled through the sample previously. The use of lenses is indispensable to correct defects, such as spherical or chromatic aberrations^{73,74}.

2.2.6 Fourier Transform Infrared Spectroscopy

Fourier Transform Infrared Spectroscopy (FTIR) has been used as analytic tool in chemistry, especially in areas of micro-analysis where high precision is important. The FTIR analysis can be carried out in liquid or solid samples. The working principle of FTIR is based in the interaction between an incident wave and the sample. An interferometer is in charge of producing the interference wave - Michelson interferometer is the most commonly used one. The data produced by the interaction is collected and stored by a computer which performs the Fourier transform in addition to spectral presentation, resolution enhancement, calibration, and calculation of correlation equations⁷⁵.

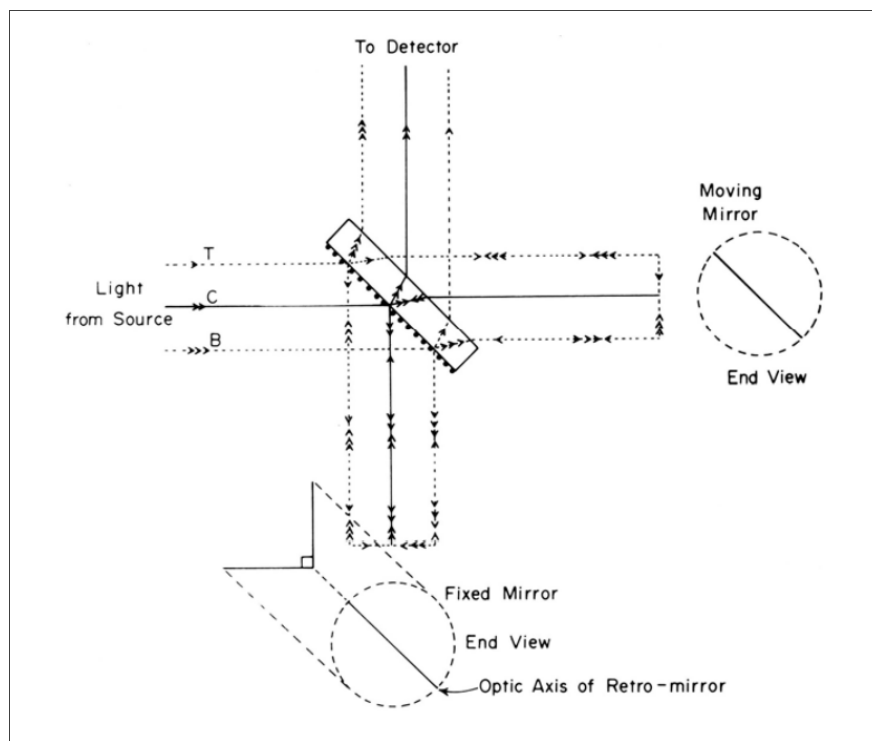


Figure 2.6: Michelson interferometer that converts an incoming infrared beam into an interference wave that interacts with the sample. Copied from Ref. 76.

The interference wave is created when an infrared beam is directed to the Michelson interferometer as shown in Figure 2.6. The incoming beam is divided by a beam splitter. Half of the beam is reflected back with a fixed mirror while the other half is reflected with a moving mirror. When both beams coming back from the mirrors are recombined, they produce a rebuilt beam that is optically an interference wave. Then, the interference wave travels through the sample where it is modified due to the interaction with the sample. Commonly, a deuterated triglycine sulfate (DTGS) pyroelectric detector detects the modified interference wave. Analog signals reached by the detector are converted to digital information and stored in the computer. A complete FTIR spectrum can be processed in a single cycle of the moving mirror. The digital data collected in first place by the computer is called interferogram. The interferogram is an electrical signal in function of time delay (retardation) of the two halves of the beams. Several number of scans are performed to reduce the signal-to-noise ratio. Finally, mathematical techniques, such as zero filling, phase correlation and apodization treat the data for the subsequent Fourier transform. With the help

of Fourier transform, the signal is converted from time domain to frequency domain using the following equation 2.9^{75,76}.

$$S(\nu) = 2 \int_0^{\infty} I(x) \cos(2\pi\nu x) dx . \quad (2.9)$$

where,

x , Retardation.

$I(x)$, Interferogram function.

$\bar{\nu}$, wavenumber.

$S(\nu)$, The spectrum in function of frequency.

Usually, the software compares the data obtained with a huge library to determine the origin of the peaks. However, the data should be compared with the literature in order to carry out a more accurate analysis.

Chapter 3

Results & Discussion

In this chapter, it will be deeply explained the materials, equipment, and protocols employed during the development of the thesis project. Additionally, discussions about the processes and analysis of results will be treated along the text. This chapter consists of two parts: synthesis and characterization. As mentioned before, the synthesis consists of two sections which are: production of PTFE fine-powder and PTFE NPs. The first subsection describe the fabrication of PTFE fine-powder, while the second subsection explains the synthesis of NPs from the PTFE fine-powder. In the characterization section, analyses, such as Diffuse Reflectance ultraviolet visible spectroscopy (UV-Vis), TEM, XRD, Fourier-Transform Infrared spectroscopy (FTIR), X-ray imaging, and ultrasound imaging, are presented.

3.1 Synthesis of PTFE Fine-powder and NPs

3.1.1 Production of PTFE Fine-powder

PTFE is well known for possessing high chemical resistance that makes it almost impossible to dissolve in any organic solvent³⁸. However, in order to synthesize NPs, various tests were performed by using several types of PTFE sources and solvents. PTFE tapes, sprays, sealants and pastes were combined with ethanol, isopropyl alcohol, and hydrofluoric acid. The solubility of different brands of PTFE tape was assessed at room temperature and pressure. Especially, hydrofluoric acid (HF) at 40% was employed as the solvent as it was reported in the literature that PTFE tape shows a slight permeability to this compound. Additionally, a PTFE spray was purchased to extract PTFE powder but it was not really satisfactory. Good

results were obtained by using the sealant “WEICONLOCK® AN 301-65 Pipe and Flange Sealing”. The following protocol was elaborated on the basis of experiments by taking a especial care of the composition of the product used to obtain PTFE powder (WEICONLOCK®). According to the safety datasheet of this product, apart of PTFE, it contains 1,4-Benzoquinone which could be broken down with acids⁷⁷.

Materials

1. WEICONLOCK® AN 301-65 Pipe and Flange Sealing provided by JEV Soluciones en Ingeniería (Quito, Ecuador)
2. Hydrofluoric acid (HF) 250 mL (38-40%) purchased from Multiciencias del Ecuador S.A
3. 2-propanol of Fisher Chemical A416P4

Methodology

To a Falcon tube of 50 mL, were added 30 mL of HF with a plastic Pasteur pipette and 15 g of WEICONLOCK®. The process was carried out inside the fume hood due to the toxicity of HF. The Falcon tube was cover with the lid and placed in the Vortexer (by Heathrow Scientific) at 2000 RPM for 15 min. Consequently to this vigorous stirring, a yellow suspension was formed which was the 1,4-Benzoquinone in a process of condensation and decomposition following the effect of the HF. Then, the tube was centrifuged to separate the PTFE from the 1,4-Benzoquinone in a Thermo Scientific™ Sorvall™ Legend™ XTR Centrifuge at 6000 RPM for 5 min. After that, a white pellet and a intense yellow supernatant were obtained. The supernatant was removed leaving the white pellet in the tube. Then, 30 mL of HF were added again and the process of mixing in the vortexer and centrifugation was repeated. Once again, a less intense yellow supernatant was formed and was removed from the tube carefully using a plastic pipette. Then, the white pellet (PTFE) was transferred to another clean tube to avoid any contamination from remaining 1,4-Benzoquinone that may be stuck to the walls of the tube. The obtained white substance was PTFE, this was washed three times using 2-propanol as follows: 15 mL of 2-propanol were added to the tube containing PTFE, subjected to shaking in the Vortexer at 2000 RPM for 10 min, then, centrifuged at 6000 for 5 min. The supernatant was removed leaving in the bottom of the tube sedimented PTFE sedimented. As mentioned, the wash process was executed 3 times. Finally, after the final washing, the sedimented PTFE was dried in a Drying oven SLW 115 POL-EKO APARATURA® at 80 °C for 6 h. Instrumentation used during this process and the paste with PTFE are shown in Figure 3.1

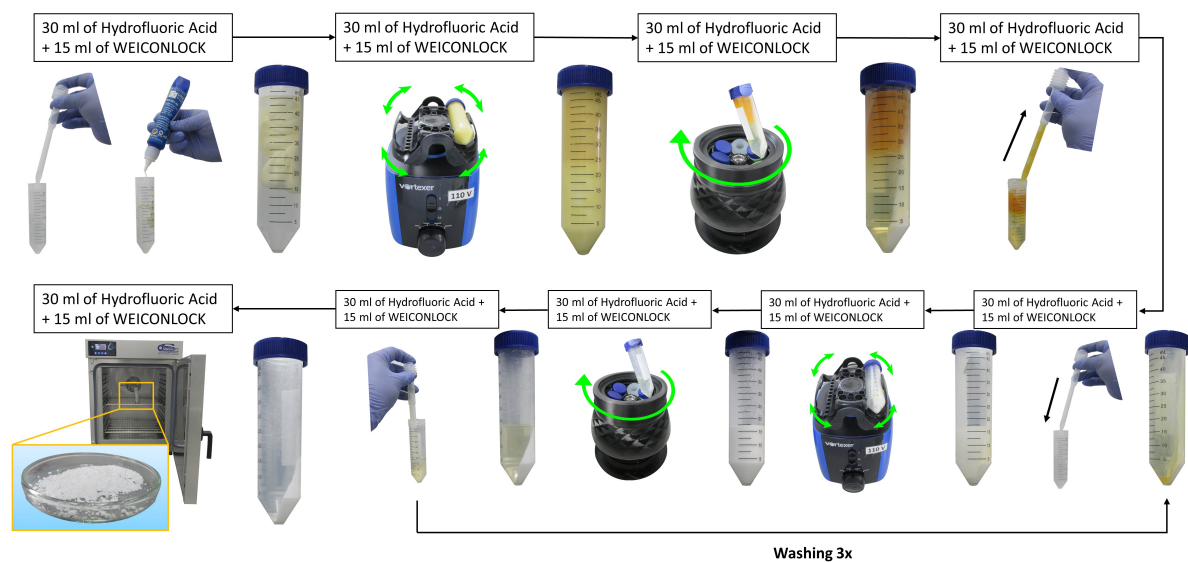


Figure 3.1: Implements and methodology employed in the synthesis of PTFE fine-powder.

3.1.2 Production of PTFE NPs

Once PTFE fine-powder was synthesized as described in subsection 3.1.1, the next step consisted in the production of PTFENPs. This was performed by dispersing the fine-powder in a solvent. The following methodology to generate homogeneous nanoparticles was planned by considering sonication and differential centrifugation as the main steps. Additionally, in order to optimize the process without many attempts, advices from Ph.D Alexis Debut were profoundly considered. For example, recommendations about the solvent and concentration of surfactant were considered *

Materials

1. Ethanol absolute CAS 64-17-5 for analysis EMSURE® ACS,ISO,Reag. Ph Eur
2. TWEEN® 80
3. PTFE fine-power (previously produced)

*Alexis Debut is Head of the Nanomaterials Characterization Laboratory Center of Nanoscience and Nanotechnology (CENCINAT) in Universidad de las Fuerzas Armadas (ESPE).

Methodology

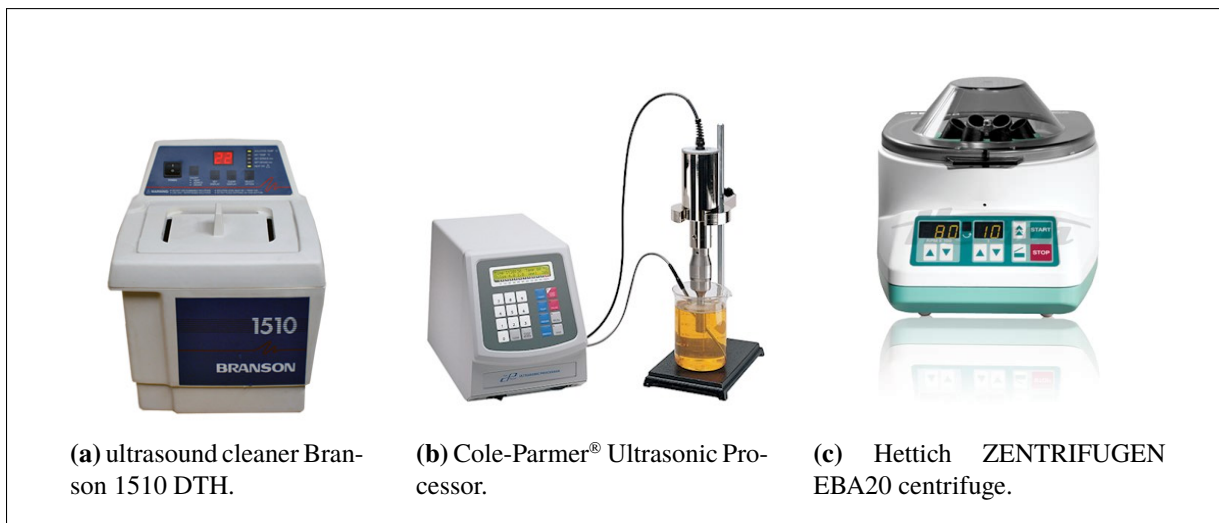


Figure 3.2: Implements employed in the production of PTFE NPs.

10 mL of ethanol were first poured into a 15 mL-Falcon tube, then 0.12 g of PTFE powder were added. The tube was sealed with the lid and hand-shaken vigorously. Immediately after that, the tube was placed into a ultrasound cleaner Branson 1510 DTH during 1 hour at room temperature. The water of the bath must cover almost the three fourths of the Falcon tube. Then, the supernatant was extracted leaving the sedimented matter in the tube. The supernatant was placed in a baker of 50 mL adding 1% (v/v) of TWEEN[®] 80 for subsequent sonication. The sonication was made with a Cole-Parmer[®] Ultrasonic Processor at an amplitude of 72% for 30 min. This system of sonication was made with a probe which was introduced directly in the solution. After that, the solution was placed back in a 15 mL-Falcon tube to perform the differential centrifugation. A centrifugate Hettich ZENTRIFUGEN EBA20 was employed for the case. It is important to put another tube with the same weight in order to balance the load. The tube was centrifuged at 6000 RPM for 30 min, then 1.5 mL of the supernatant was taken carefully and placed in another recipient. The supernatant obtained was almost transparent as it contains the PTFE NPs which was subjected to several techniques of characterization.

3.2 Characterization of PTFE Fine-powder and NPs

3.2.1 Diffuse Reflectance UV-Vis Spectroscopy of PTFE Fine-powder

This technique is useful to analyze powders. Thus, it is perfect to determine the properties of PTFE fine-powder⁶⁴. The device employed for this measurement was a LAMBDA 1050 UV-Vis Spectrophotometer PerkinElmer[®] that includes the PerkinElmer[®] accessory 3D WB Detector Module. However, in order to analyze the powder, the Praying Mantis[™] Diffuse Reflection Accessory was used. The light spot was about 1-2 mm. The PTFE powder was filled to the sample holder: a hole of 10 mm in diameter and 3 mm depth, and the surface was smoothed. Prior to performing the analysis, white standard of BaSO₄ was used as a blank.

Diffuse Reflectance UV-Vis spectroscopy was carried out in the fine-powder to determine the optical properties of this material as shown in Figure 3.4 a). The PTFE is capable to absorb electromagnetic radiation under the visible spectrum. Therefore, the minimum energy at which electronic transitions occurs was analyzed.

First, the diffuse reflectance UV-Vis spectrum was fitted to determine accurately the wavelength at which the PTFE powder begins to absorb the electromagnetic radiation. The Boltzmann model was employed for the case using the range from 250 nm to 568 nm. A total of 6 iterations were performed before converging. The final result obtained was useful to determine the wavelength where the reflectance drops abruptly.

$$y = A_2 + \frac{A_1 - A_2}{1 + e^{\frac{x-x_0}{dx}}} , \quad (3.1)$$

The final values obtained after fitting are the following:

Table 3.1: Data obtained post-fitting of UV-Vis spectrum of PTFE fine-powder

Parameter	Value	Standard error
A_1	2.19	0.081
A_2	45.63	0.082
x_0	410.20	0.158
dx	7.71	0.137

The results point out that electronic transitions, deflection of the curve, starts at about 410.2 nm as shown in Table 3.1 parameter x_0 . Then, the reflection was almost zero for values below 410 nm. This

approximation was useful to know the approximately value at which electronic transitions occurs. However, another analysis was performed to determine the band gap accurately.

Kubelka-Munk Transformation

The value of the band gap was determined using the K-M transformation⁷⁸. In order to transform the reflectance to K-M, the wavelength of x-axis was converted to energy by using the Einstein-Planck relation⁷⁹ in equation 3.2:

$$E = h\nu = h\frac{c}{\lambda}, \quad (3.2)$$

where,

h , Planck constant. (6.62×10^{-34} Joule \cdot s = 4.135667×10^{-15} eV \cdot s)

ν , Frequency.

λ , Wavelength.

c , Speed of light (299792458 m/s = $2.99792458 \times 10^{17}$ nm/s).

Then the reflectance was converted to the so called remission or Kubelka-Munk function (k/s) ⁷⁸.

$$\frac{k}{s} = \frac{(1 - R)^2}{2R}, \quad (3.3)$$

where,

k , Absorption coefficient.

s , Scattering coefficient.

R , Reflectance.

Finally, a plot with $h\nu$ along x-axis and $[(k/s)h\nu]^2$ along y-axis was made. The value of the band gap was determined by extrapolating the straight line in the graph at $k = 0$ ⁷⁸ as shown in Figure 3.4 **b**).

The results of this analysis suggest that PTFE fine-powder can absorb electromagnetic radiation below the visible spectrum and the powder acts as insulator with a band gap equal to 3.27 eV. Then band gap is the energy gap between the valence and conduction bands. In the valence band are located the electrons with the highest energy levels. Electronic transitions occurs when electrons flow from valence to conduction. The valence electrons need additional kinetic energy to flow to conduction band, which is given by the electromagnetic radiation during the UV-Vis analysis. Therefore, in order to move electrons from valence

to conduction band, the administered energy must be equal or greater than the band gap value⁸⁰. In the case of PTFE, electronic transitions occur with energies higher than 3.27 eV or lower than $\lambda=379.05$ nm. When these conditions are satisfied, the PTFE fine powder begins to absorb (no-reflectance) the incident electromagnetic radiation. These properties can be exploited for medical applications when ultraviolet absorbance of an insulator will be necessary.

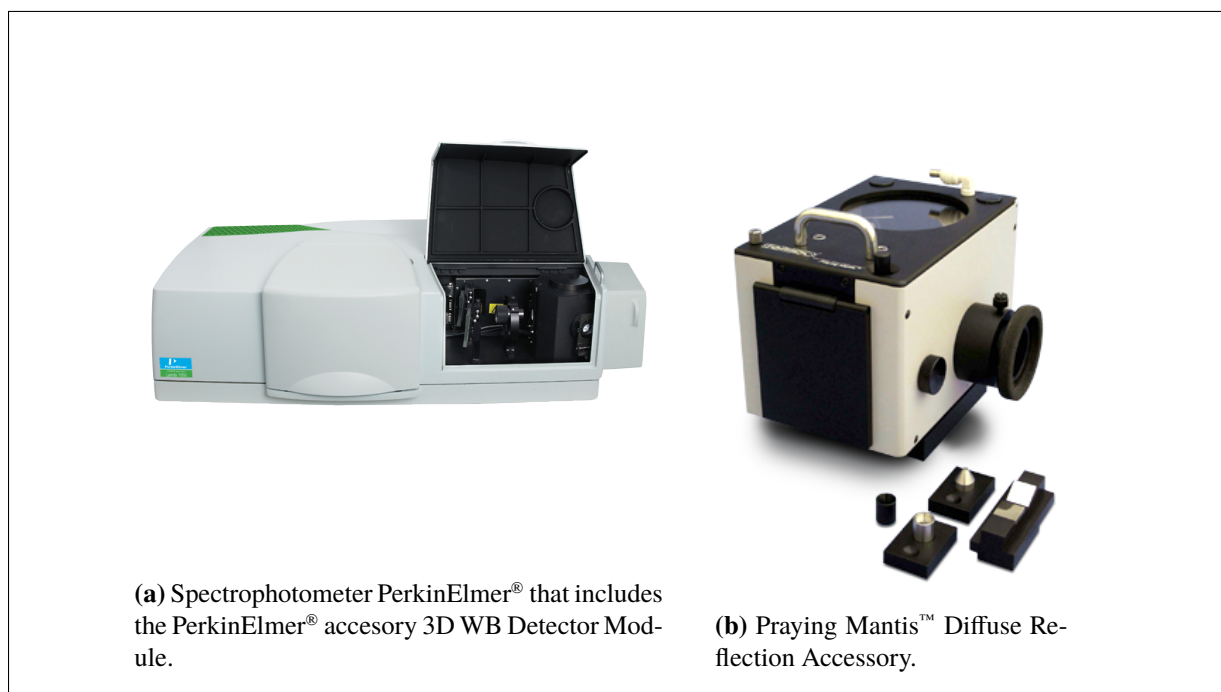


Figure 3.3: Instruments used for the diffuse reflectance UV-Vis analysis of Teflon[®] powder.

3.2.2 X-ray Powder Diffraction of PTFE Fine-powder

X-ray Diffraction (XRD) patterns were carried out on a PANalytical brand $\theta - 2\theta$ configuration (generator-detector) X-ray tube, with Cu $K\alpha$ irradiation $\lambda = 1.54059$ Å and EMPYREAN diffractometer. In the XRD pattern of fine PTFE powder, it is possible to observe the characteristic peaks of this fluoropolymer; however, there exist a contamination, which is determined by the presence of extra peaks of rutile (TiO_2) as shown in Figure 3.5. The XRD pattern was analyzed to determine the space between planes, the crystalline size, and the background was deconvoluted to determine the percentage of crystallinity.

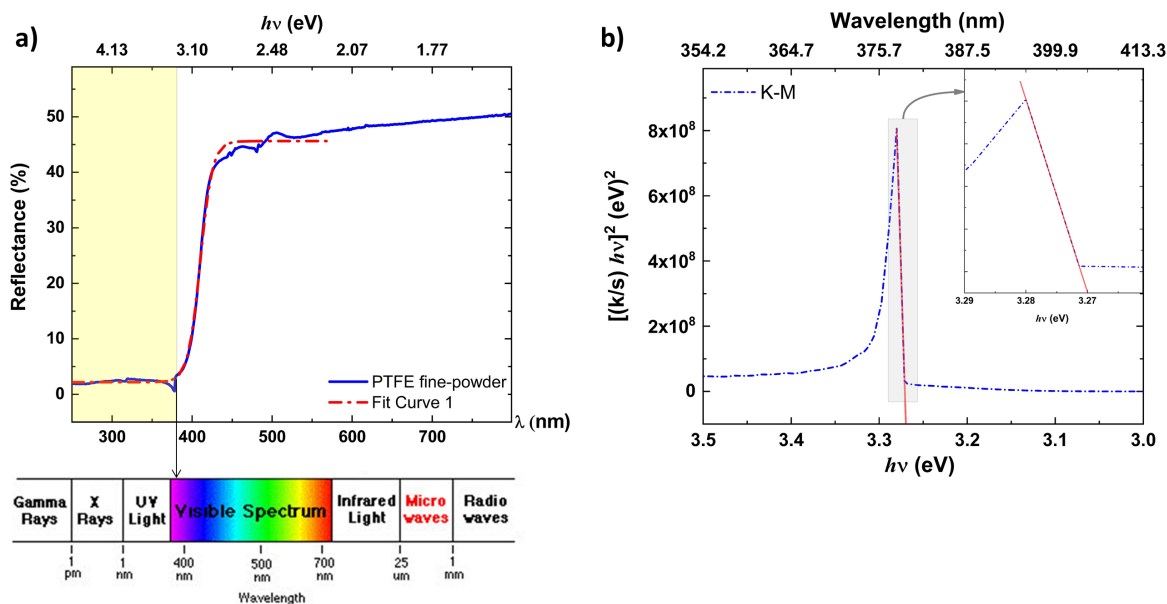


Figure 3.4: a), Diffuse Reflectance UV-Vis Spectroscopy spectrum of PTFE fine-powder and its fitting with the range of electromagnetic radiation at which this material witnesses electronic transitions. b), Kubelka-Munk transformation of DRS to determine the band gap precisely.

Bragg's Law

This equation is useful to determine the distance between planes of the same family. It assumes that planes in the lattice diffracts the X-rays continuously. The interplanar distance is useful to determine the constants of the unit cell of PTFE⁸¹. By using Origin, it was possible to determine the position of PTFE peaks.

$$n\lambda = 2d \sin\theta \quad , \quad (3.4)$$

where,

- n , Integer number known as order of reflection. In this case was 1.
- λ , Wavelength of the X-rays (0.154059 nm).
- d , distance between crystal planes.
- θ , angle at which peaks of PTFE are observed, that are shown in Table 3.2.

The interplanar distances (d-spacing) calculated for PTFE are shown in Table 3.2. With the help of

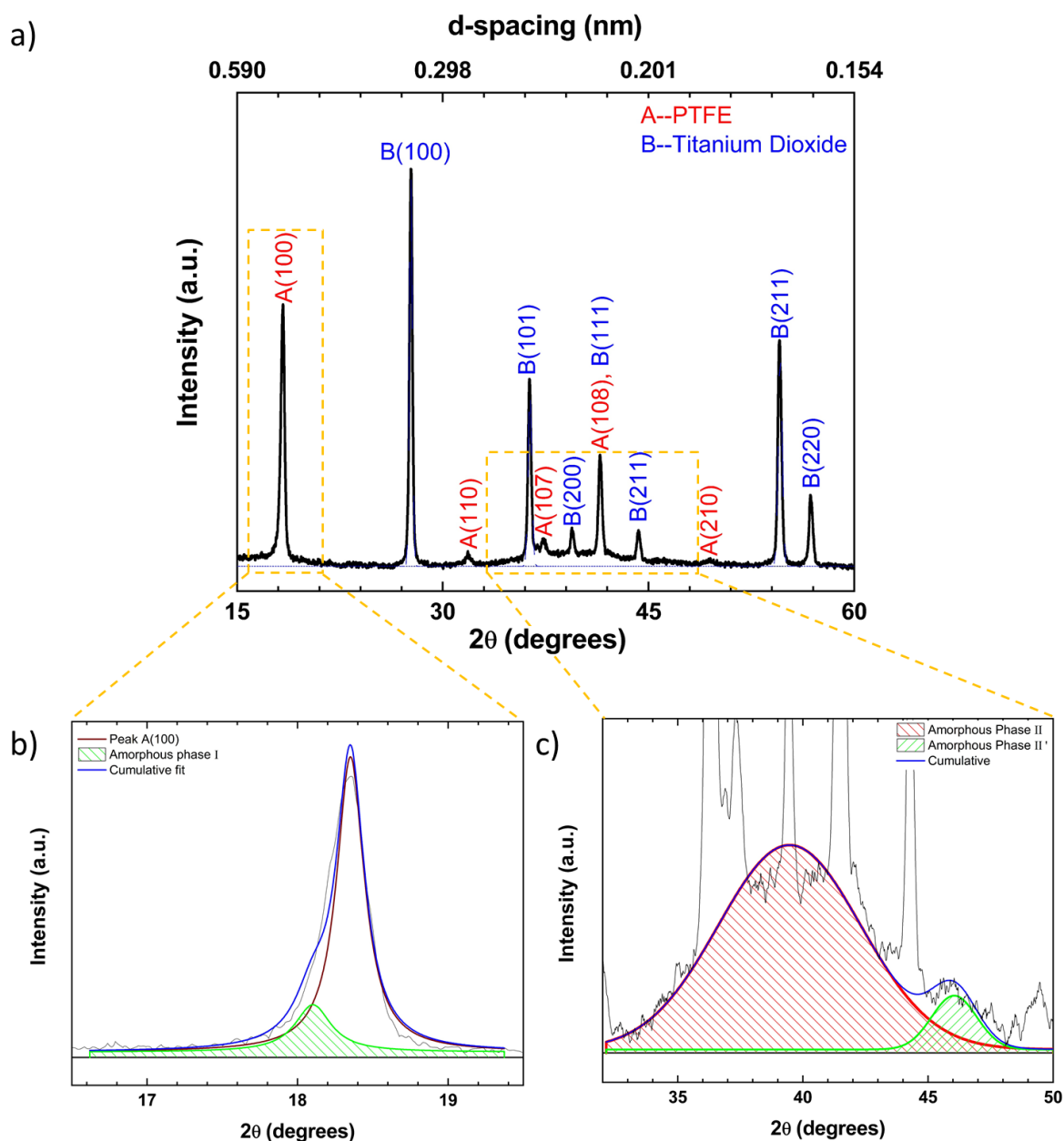


Figure 3.5: XRD pattern of PTFE fine-powder. **a)** Miller indexes assigned to the corresponding peaks of PTFE and the contamination (TiO_2). The top axis was calculated to show the scale in d - spacing (nm), while the bottom axis displays the well known 2θ units in degrees. **b)** The main peak (100) of PTFE was deconvoluted into 2 peaks with Lorentzian functions to determine the percentage of amorphous phase I in the fine-powder. **c)** The background, known as amorphous phase II, was deconvoluted with Gaussian functions to determine the percentage of amorphous phase II. Both peaks were seen due to amorphous phase II, however, the bigger peak represents the intramolecular scattering (Amorphous Phase II), while the smaller peak comes from interatomic scattering (Amorphous Phase II').

this information and the use of crystal geometry equation for hexagonal lattice, the lattice parameters are calculated. It is important to consider that 15₇ helical PTFE chains are conforming in a hexagonal lattice²⁹, therefore the axial lengths and angles are: Two equal coplanar axes at, 120° third axis at right angles⁸².

$$a = b \neq c, \alpha = \beta = 90^\circ, \gamma = 120^\circ$$

Miller indexes for peaks of PTFE were compared with the literature to determine the correct planes for each intense peak as shown in Table 3.2²⁹. Additionally, the intensities of the peaks were determined by comparing each peak with the most intense peak in the XRD spectrum (100), the information of the intensities is shown in Table 3.2.

Table 3.2: Description of peaks observed in the XRD pattern for PTFE with their corresponding Miller indexes (hkl), interplanar space (d-spacing), position (2θ), and relative intensities (I/I_o) with respect to the higher peak (100).

(hkl)	d-spacing (nm)	2θ (degrees)	I/I_o
100	0.483051	18.35163	100%
110	0.280909	31.83053	14.2%
107	0.240496	37.36138	18.7%
108	0.217552	41.47344	47.4%
210	0.184113	49.46485	11.4%

Crystal Geometry Equation for Hexagonal Lattice

Then, by using the data of Table 3.2, it is possible to determine the lattice parameters for the hexagonal crystal structure of PTFE using the following equation⁶⁶:

$$\frac{1}{d^2} = \frac{4}{3} \left(\frac{h^2 + hk + k^2}{a^2} \right) + \frac{l^2}{c^2} \quad (3.5)$$

Already, we know the interplanar space (d-spacing) and Miller indexes, thus the lattice parameter a was calculated by using the plane (100) with its $d - spacing = 0.483051$ nm in the equation 3.5:

$$\frac{1}{0.483051^2} = \frac{4}{3} \left(\frac{1^2 + 0 \cdot 0 + 0^2}{a^2} \right) + \frac{0^2}{c^2} ,$$

Solving for a ,

$$a = \sqrt{\frac{4 \cdot 0.483051^2}{3}} = 0.557779 \text{ nm} ,$$

Then, the lattice parameter, c , was calculated by using the plane (107) with its d - spacing = 0.240496 nm and the lattice parameter a , previously calculated, in 3.5:

$$\frac{1}{0.240496^2} = \frac{4}{3} \left(\frac{1^2 + 1 \cdot 0 + 0^2}{0.557779^2} \right) + \frac{7^2}{c^2} ,$$

Solving for c ,

$$c = \sqrt{\frac{49 \cdot 4 \cdot 0.240496^2}{3 \cdot 0.557779^2}} = 3.485081 \text{ nm} ,$$

In summary, the PTFE is a short range 15_7 helical structure within the individual polymer chains that conform a long range hexagonal packing structure between chains with the following parameters that can be shown in Figure 3.6. All the reflected planes are sketched which also are tagged in the XRD pattern in Figure 3.5 a).

$$\begin{aligned} a &= b = 0.557779 \text{ nm} \\ c &= 3.485081 \text{ nm} \\ \alpha &= \beta = 90^\circ \\ \gamma &= 120^\circ \end{aligned}$$

Percentage of Crystallinity

The percentage of crystallinity can be determined by using the XRD pattern. The crystallinity is obtained quantitatively by comparing the ratios between the area of the crystalline peaks and the background. The sharp peaks means the presence of a crystalline phase while the broad peaks reveals the existence of an amorphous phase. The area of the peaks and the background are calculated using the following equation:

$$\% \text{ Crystallinity} = \frac{\text{Area of crystalline peaks}}{\text{Total Area (Crystalline+Amorphous)}} \cdot 100\% = \frac{4035.832}{5196.373} \cdot 100\% = 77.7\% \quad (3.6)$$

PTFE presents two amorphous components in addition to the crystalline one. One of the amorphous phases is present around the peak (100), and the second at an angle about of 40° ⁸³. Therefore, these areas were deconvoluted to obtain the area and consequently the amorphous percentage. The peak (100) was

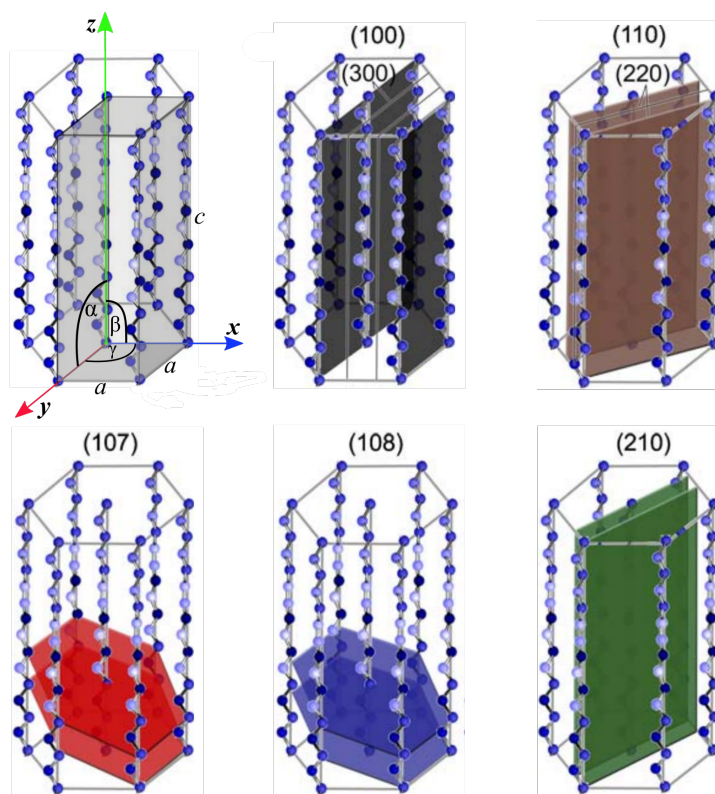


Figure 3.6: Unit cell of PTFE packaged by chains of CF_2 in a hexagonal lattice. Additionally, the unit cell is repeated by pointing the planes to compare with XRD pattern. Adapted from Ref. 29.

deconvoluted using OriginPro software by using Lorentzian functions as shown in Figure 3.5 b), then by using the area calculated, the quantitative analysis was performed. The amorphous phase at about 40° was deconvoluted by using Gaussian functions as shown in Figure 3.5 c).

Table 3.3: Description of peaks observed in the XRD pattern for PTFE with their corresponding Miller indexes, interplanar space, position, and relative intensities with respect to the more intense peak (100).

	Amorphous Components				Crystalline Component	Total
	Unknown	Phase I	Phase II	Phase II'		
Area	87.188	160.468	842.831	70.054	4035.832	5196.373
Percentage (%)	1.678	3.088	16.220	1.348	77.666	100%

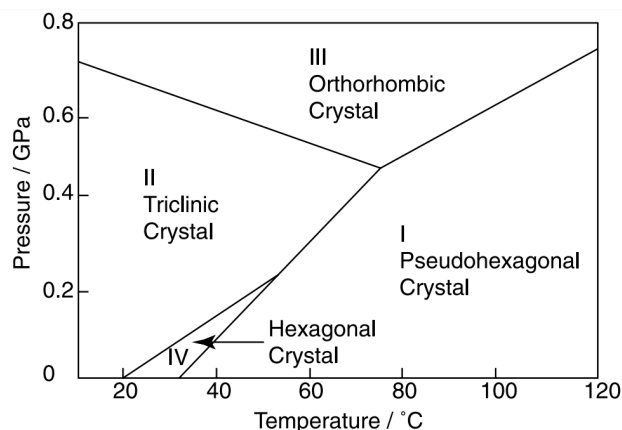


Figure 3.7: Phase diagram of PTFE for different values of temperatures and pressures. PTFE is commonly presented in phase IV represented by a hexagonal crystal. However, phases I and II can be joined to the phase IV in an amorphous type. Copied from Ref. 84.

The percentages of crystallinity and the amorphous components are presented in Table 3.3, which were calculated quantitatively with the ratios between crystalline peaks and deconvoluted background. However, there is an unknown amorphous component of 1.678% that can be attributed to the noise and problems with the fitting. In summary, the results displayed in Table 3.3 present different amorphous components due to tangled chains of PTFE. The peaks of PTFE represent a phase IV (hexagonal crystal), but there is a total amorphous phase I (triclinic crystal) of 3.088% at about 18°, that is originated of intermolecular scattering. The amorphous phases II and II' (pseudohexagonal crystal), characterized by a diffuse scattering, are in the same range at about 40°. All phases that PTFE can acquire are presented in the phase diagram in Figure 3.7⁸⁴. Therefore, there are 16.220% of amorphous phase II, shown in Figure 3.5 c), that corresponds to intramolecular scattering. Moreover, 1.348% of amorphous phase II' are observed corresponding to the interatomic scattering of the fine-powder⁸³.

Crystalline Size

P. Scherrer observed that the diffracted beam of monochromatic radiation falling into a crystal can be broadened with small particles. Scherrer equation relates the broadening of a peak in the XRD pattern with the particle size. This expression is written in the following form⁸⁵:

$$B = K\lambda / (L \cos \chi/2) , \quad (3.7)$$

where,

- B , is the line broadening at full width at half maximum (FWHM).
 λ , wavelength of the incident X-rays (0.154059 nm).
 K , numerical constant equal to $2(\ln 2/\pi)^{\frac{1}{2}} = 0.93$.
 $\chi/2$, Bragg angle at which peaks of PTFE are observed, that are shown in Table 3.2.
 L , the linear dimension of the particle.

Table 3.4: Correlations between diffraction peak aberrations, broadening, shifts or asymmetries, and the different elements of microstructure. Copied from Ref. 86.

	Peak Aberrations				
	Peak Shift	Peak Broadening	Peak Asymmetry	Anisotropic Peak Broadening	Peak Shape
<i>Dislocations</i>		+	+	+	+
<i>Stacking Faults</i>	+	+	+	+	+
<i>Twinning</i>	+	+	+	+	+
<i>Microstresses</i>		+			
<i>Long-Range Internal Stresses</i>	+		+		
<i>Grain Boundaries</i>	+	+			
<i>Sub-Boundaries</i>	+	+			
<i>Internal Stresses</i>	+				
<i>Coherency Strains</i>	+	+	+		
<i>Chemical Heterogeneities</i>	+	+	+		
<i>Point Defects</i>				+	
<i>Precipitates and Inclusions</i>			+		+
<i>Crystallite Smallness</i>		+		+	+

With equation 3.7, it is possible to calculate the particle size. For this purpose, the most intense peak (100) is selected whose FWHM (2θ) is equal to 0.22339, the wavelength of X-rays is 0.154059 nm, and the peak position (2θ) is 18.35163. Before performing the calculations, the values of FWHM and peak position must be converted to radians by multiplying the angle with $\pi/180$. For example, $1^\circ \cdot \pi/180 = 0.01745$ rad. The values converted are introduced in the equation 3.7 as:

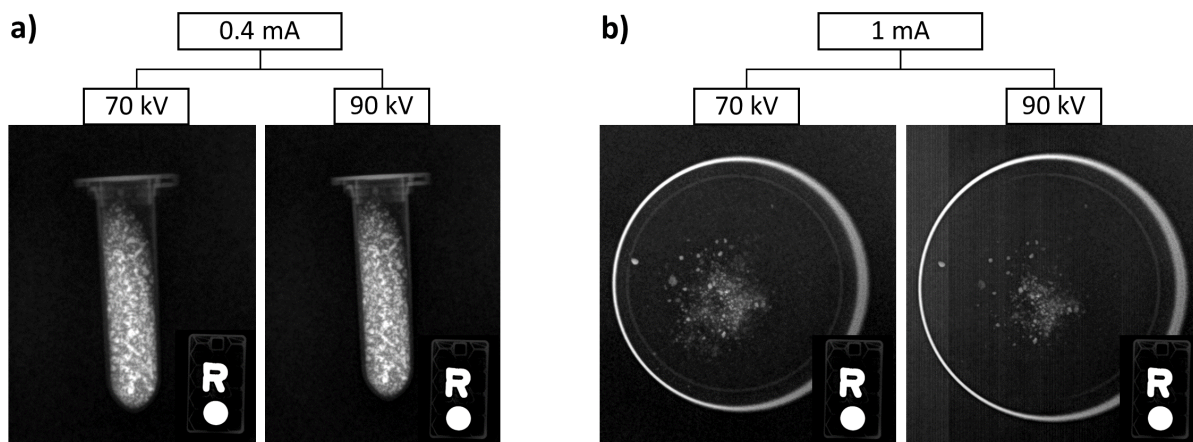


Figure 3.8: X-ray Imaging of PTFE fine-powder. **a)** shows eppendorf tubes of 2 mL filled with powder, which were subjected to different potentials with the same current. **b)**, it shows a top view of a small amount of PTFE fine-powder dispersed in a petri dish.

$$0.003899 = 0.93 \cdot 0.154059 / (L \cos 0.16048/2)$$

Solving for L ,

$$L = \frac{0.93 \cdot 0.154059}{\cos 0.16048/2} = 36.02 \text{ nm}$$

The particle size obtained through the use of Scherrer equation is not related with the TEM images where the average size are 105 nm and 14 nm (see below). This problem comes from the statement that peak broadening changes due to several factors in addition to the grain size, which are enlisted in the Table 3.4⁸⁶.

3.2.3 X-ray Imaging of PTFE Fine-powder

The X-ray attenuation properties of PTFE fine-powder was evaluated in eppendorf and petri dishes with a micro-CT scanner (1076 Skyscan, Kartuizersweg, Belgium). Experimental parameters were as follows: X-ray, 70 kV, 90kV, 0.4 mA, 1 mA; resolution, 35 μ m; pitch, 0.4; aluminum filters, 0.5 and 632 ms.

PTFE powder exhibits a X-ray attenuation which is supported by the contrast observed in the images of Figures **a)** and **b)** in 3.8. In figure **a)** it is possible to observe that PTFE attenuates X-rays of different

energies (potential) with the same intensity. Interestingly, in **b)** the dispersed powder in petri dishes point out that the attenuation is intrinsic to PTFE and the thickness of the sample does not influence it. In summary, the powder was subjected to different parameters by tuning the tube current and potential. As an outcome, these parameters do not affect the X-ray attenuation. This result points out that PTFE fine-powder is capable to absorb electromagnetic radiation of high energy (X-rays) at different conditions without affecting the attenuation.

3.2.4 Ultrasound Imaging of PTFE Fine-powder

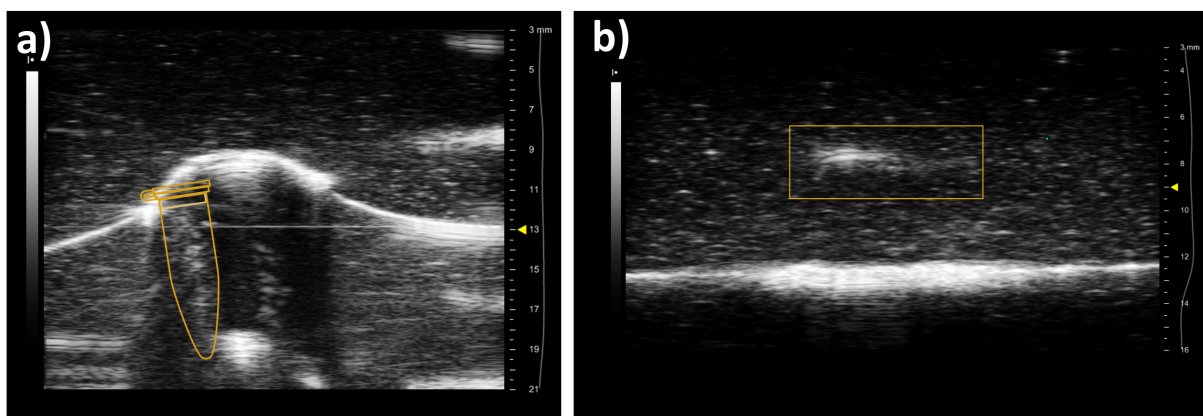


Figure 3.9: Ultrasound imaging of PTFE fine-powder. **a)**, shows the eppendorf tube filled with PTFE powder. **b)** shows a small amount of powder dispersed in a container which is highlighted with a yellow box.

US imaging was performed at the Mouse Clinical Institute using a preclinical Vevo 2100 echographer and computer (Visualsonics, Toronto, Ontario, Canada). The parameters employed were: frequency, 21 MHz; power, 100%; acquisition depth and width of 16 mm and 23.04 mm, respectively.

The ultrasound test demonstrated that the as-produced PTFE fine-powder absorbs the ultrasound as mentioned in the literature^{57,58}. With this analysis, it was possible to point out that PTFE demonstrates awesome properties to absorb ultrasound. One test was performed with an eppendorf tube filled with PTFE fine-powder and subjected to the US imaging as shown in Figure 3.9 **a)**. In this image, clearly the powder produces a contrast that is observed by the white spots produced inside the eppendorf tube. A second test of US attenuation was performed where the powder was taken out of the tube and placed in a flat recipient

as shown in Figure 3.9 **b**). This second test manifested that the attenuation was produced exclusively by the PTFE powder and the plastic tube does not interfere. Additionally, it is possible to mark that the contrast produced is almost the maximum intensity. Both images clearly point out the attenuation of US by the PTFE dust. This outstanding property can be exploited in theranostic and imaging applications.

3.2.5 Transmission Electron Microscopy of PTFE NPs

TEM images were digitally recorded for morphological studies (FEI Tecnai, G2 Spirit TWIN). PTFE NPs in colloidal solution were analyzed to determine the average size. The images were taken prior and after differential centrifugation.

TEM images were subjected to a nanoparticle size distribution analysis by using ImageJ software. Each image was treated with a band pass filter and threshold for better analysis. ImageJ generates a .CSV file with information about the area of the NPs. From the area, the diameter was calculated by using the equation for the area of a circle, as the PTFE NPs are round-shaped.

$$A = \pi r^2 ,$$

Then, from the radii of the NPs, the diameter is calculated by using the next relationship: $d = 2r$. With the data of the diameter, a histogram is generated by using OriginPro software fitted with a Gaussian function to determine the average size precisely.

Table 3.5: Size distribution of PTFE NPs analyzed in Figures 3.10 (before centrifuging) and 3.11 (after centrifuging). For each image is presented the average size, total counts, and the range of size at which the majority of NPs belong.

Figure	Average Size (nm)	Total Counts	Majority	
3.10, a)	225.6 & 406.5	8	[225 nm - 405 nm]	75%
3.10, b)	244.5 & 386.2	11	[245 nm - 385 nm]	90.1%
3.11, a)	14.05	513	[11 nm - 19 nm]	89.3 %
3.11, b)	30.4 & 111	81	[30 nm - 110 nm]	85.2 %
3.11, c)	104.9	123	[90 nm - 130 nm]	78.9 %

TEM micrographs show a huge difference in size of NPs between samples prior and after differential centrifugation. For example, Figure 3.10 **a**) displays round-shapes particles with a huge size that are in the range of 225.6 nm - 406.5 nm. Similarly, Figure 3.10 **b**) presents enormous agglomerated particles

that can not be considered as NPs rather microparticles (μ Ps). This result suggests that sonication is not enough to obtain NPs despite the high energy to which the samples were subjected. In both images of Figure 3.10, it is possible to observe agglomerates of PTFE which could not be separated with sonication. Therefore, PTFE fine-powder contains particles agglomerations bound together with high vdW, capillary, or electrostatic forces that cannot be broken down with sonication.

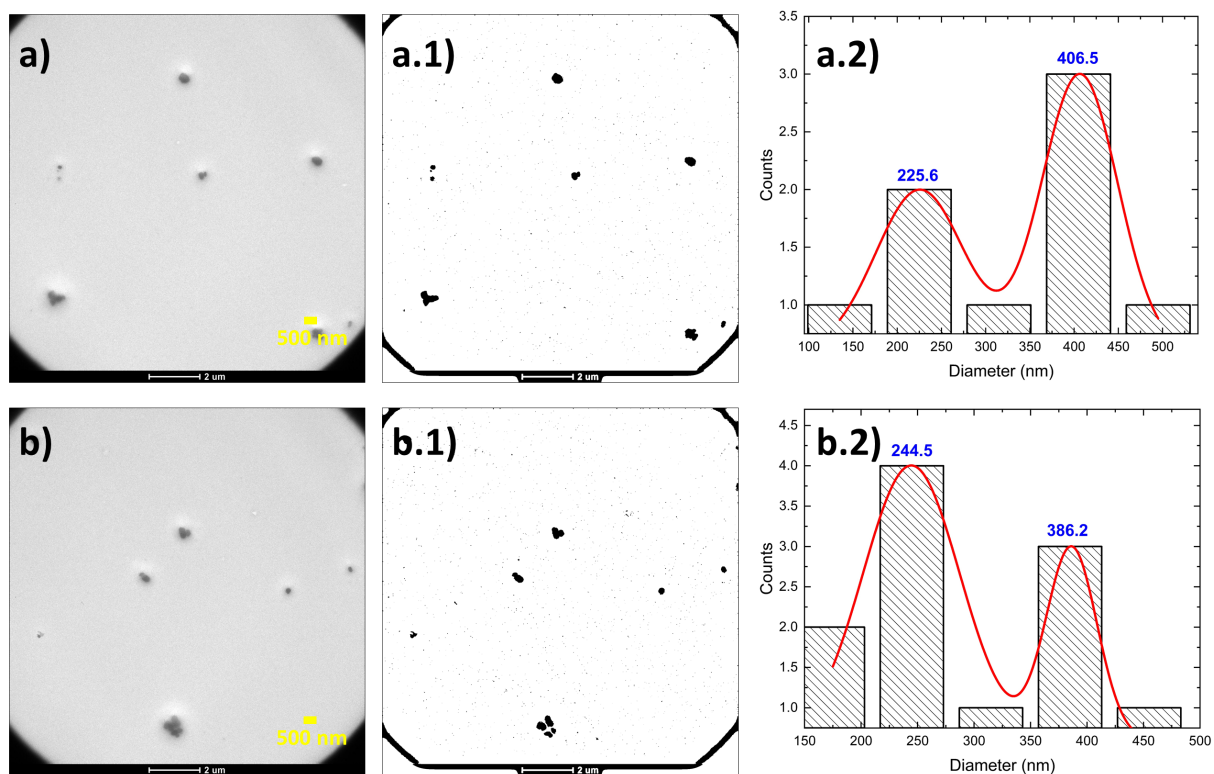


Figure 3.10: TEM images of PTFE NPs in colloidal dispersion prior to differential centrifuging. The first column are images from TEM where the PTFE NPs are the black spots. The second column are the images processed in ImageJ to eliminate the background by using different artifacts. Finally, the third column contains the histogram plots where the average sizes of PTFE NPs. Each row corresponds to one TEM image analyzed.

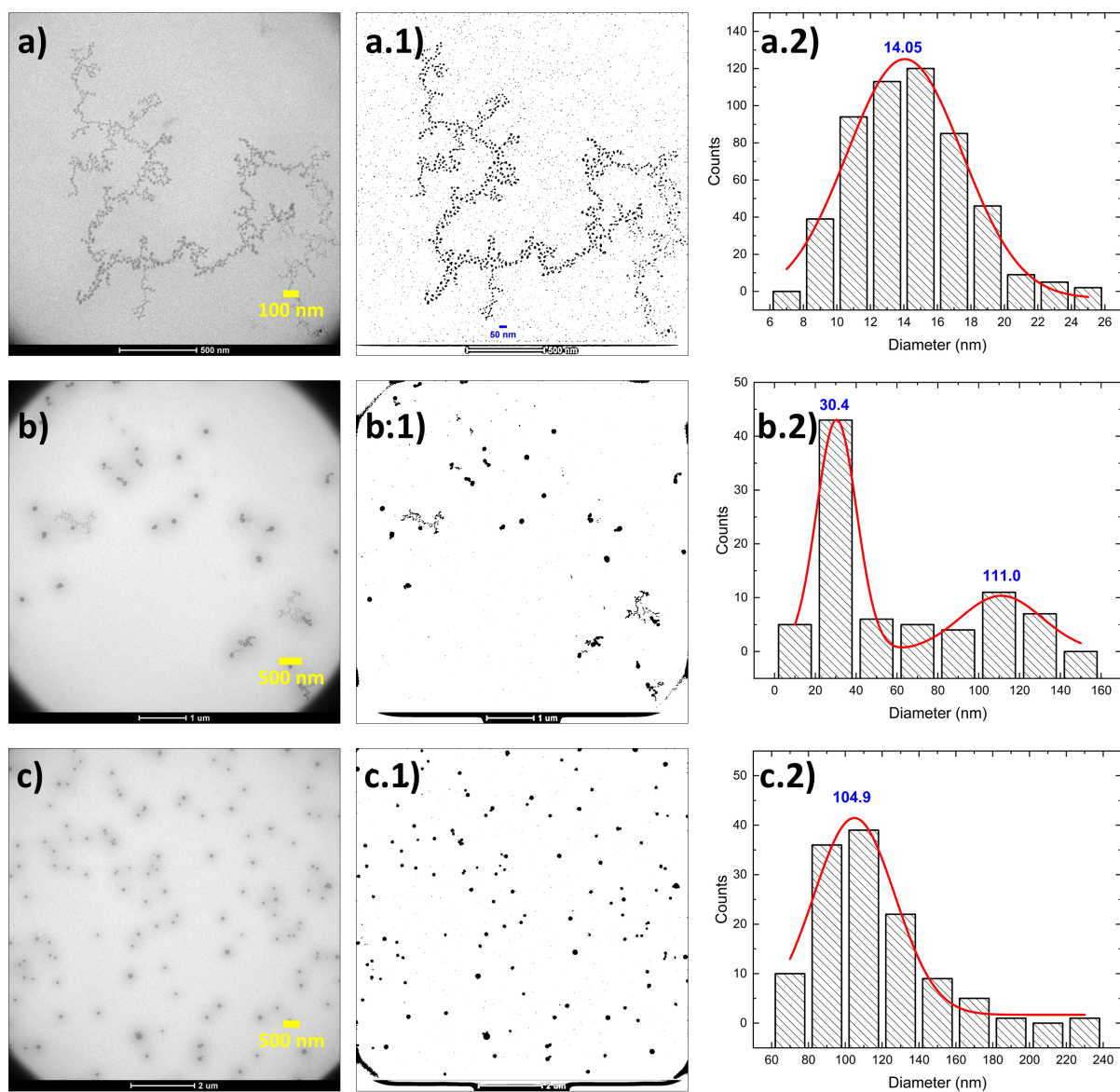


Figure 3.11: TEM images of PTFE NPs in colloidal solution after differential centrifuging. The first column are images from TEM where the PTFE NPs are the black spots. The second column are the images processed in ImageJ to eliminate the background by using different artifacts. Finally, the third column contains the histogram plots where the average sizes of PTFE NPs. Each row corresponds to one TEM image analyzed.

On the other hand, TEM images of colloidal solution after differential centrifugation demonstrates that NPs can be separated from agglomerates easily. For example, images **a**), **b**) and **c**) of Figure 3.11 belong to the same sample which was centrifuged at 6000 RPM for 30 min. In these images, it is possible to observe NPs with different sizes; for instance, Figure **b**) shows two distinct populations. As observed in Figure b.2), one population has an average size of 30 nm and the second one has 111 nm. These two populations are clearly observed between images **a**) and **c**), in image **a**) is notable the presence of small and stable NPs with an average size of 14.05 nm, while image **c**) presents NPs with a bigger size of 104.9 nm.

With these results, it is possible to point out that the surfactant Tween-80 at 1% v/v is enough to stabilize the NPs. When the concentration of surfactant exceeds this percentage, TEM is not possible to be performed as a thick film of surfactant is created that blurs the TEM images. The data of TEM images are summarized in Table 3.5 where is presented the information about the average size, total counts, and the range of size at which the majority of NPs belong to.

3.2.6 Fourier Transform Infrared Spectroscopy of PTFE NPs

Attenuated total reflectance-Fourier transform infrared spectroscopy (ATR-FTIR) was acquired on PTFE NPs at 650-4000 cm^{-1} by using a Spectrum 100 IR spectrometer (Perkin Elmer, USA). This technique is useful to determine the functional groups present in the colloidal solution and their possible interaction with the liquid media. The FTIR spectroscopy was carried out for the colloidal solution containing PTFE NPs, ethanol, and Tween-80. In addition, the spectra for ethanol, Tween-80, and rutile (TiO_2) were acquired from the literature and added to the plot for comparison. Tween-80 spectrum was obtained from NIST database (CAS: 1338-43-8)⁸⁷, FTIR spectrum of ethanol was founded in Database of ATR-FT-IR spectra of various materials⁸⁸, and rutile spectrum was obtained from RRUFF (ID: R110109)⁸⁹. Both spectra were digitized online with WebPlotDigitizer and normalized by using the intensity of the peak corresponding to O-H stretching.

The infrared spectrum of PTFE NPs + Ethanol + Tween-80 shown in Figure 3.12 **a**) contains all the characteristic peaks of ethanol and Tween-80. Additionally, peaks of PTFE were founded in the spectrum. In Figure 3.12 **b**), there is a weak peak at 1710 cm^{-1} that correspond to vibrations of $\text{C}=\text{CF}_2$ or $\text{CF}=\text{CF}_2$ ⁹⁰. A characteristic peak of PTFE is exhibited at 1236 cm^{-1} and an small shoulder at 1149 cm^{-1} that corresponds to asymmetrical stretching and symmetrical stretching of CF_2 , respectively (shown in Figure 3.12 **b**))⁹¹⁻⁹³. In Figure 3.12 **c**), two peaks appear at 730 cm^{-1} and 936 cm^{-1} that corresponds to CF_3 and $\text{CF}=\text{O}$ vibrations⁹⁰. The peaks at 589 cm^{-1} -633 cm^{-1} comes from rocking, wagging and bending

vibrational modes of CF_2 ⁹¹. In addition, the peaks at this range (589 cm^{-1} - 633 cm^{-1}), shown in Figure 3.12 **c**), are associated with the laevorotatory and dextrorotatory chirality of the PTFE structure⁹⁰.

The peaks observed at 589 cm^{-1} - 633 cm^{-1} for PTFE NPs + Ethanol + Tween-80 demonstrate the helical structure of the PTFE and the partial crystalline structure of the PTFE NPs⁹⁰. Vibrations at 1710 cm^{-1} ($\text{C}=\text{CF}_2$ or $\text{CF}=\text{CF}_2$), 730 cm^{-1} (CF_3), and 936 cm^{-1} ($\text{CF}=\text{O}$) suggest the presence of contaminants in the PTFE NPs⁹⁰.

The infrared spectrum for ethanol and PTFE NPs + Ethanol + Tween-80 shown in Figure 3.12 **a**), contains the same peaks at the same wavenumber. For example, at 3327 cm^{-1} is observed the peak from O-H stretching, while at 2975 cm^{-1} and 2890 cm^{-1} are present the peaks from C-H stretching^{94,95}. Additionally, a peak from C=C stretching appears at 1644 cm^{-1} ⁹⁶. Finally, three peaks from C-O stretching are present at 1381 cm^{-1} , 1088 cm^{-1} , and 1043 cm^{-1} ^{94,95}, which comes from functional groups of Tween-80.

Table 3.6: Frequencies (cm^{-1}) of main peaks observed in the FTIR spectrum with their corresponding vibrational modes.

ν (cm^{-1})	Type of vibrational mode	Functional group	References
1710	Vibrations	$\text{C}=\text{CF}_2$, $\text{CF}=\text{CF}_2$	90
1236	Asymmetrical Stretching	CF_2	91,92
1149	Symmetrical Stretching	CF_2	91-93
936	Vibrations	CF_3	90
730	Vibrations	$\text{CF}=\text{O}$	90
633	Rocking, Wagging, and Bending	CF_2	91
589	Rocking, Wagging, and Bending	CF_2	90,91
3327	Stretching	O-H	94,95
2975	Stretching	C-H	94,95
2890	Stretching	C-H	95
2350	Asymmetric Stretching	CO_2	97
1736	Stretching	$\text{C}=\text{O}$	98
1644	Stretching	$\text{C}=\text{C}$	96
1381	Stretching		94,95
1088	Stretching	C-O	94,95
1043	Stretching		94,95
880	Bending	C-H	94,95
610	Stretching	Ti-O	99

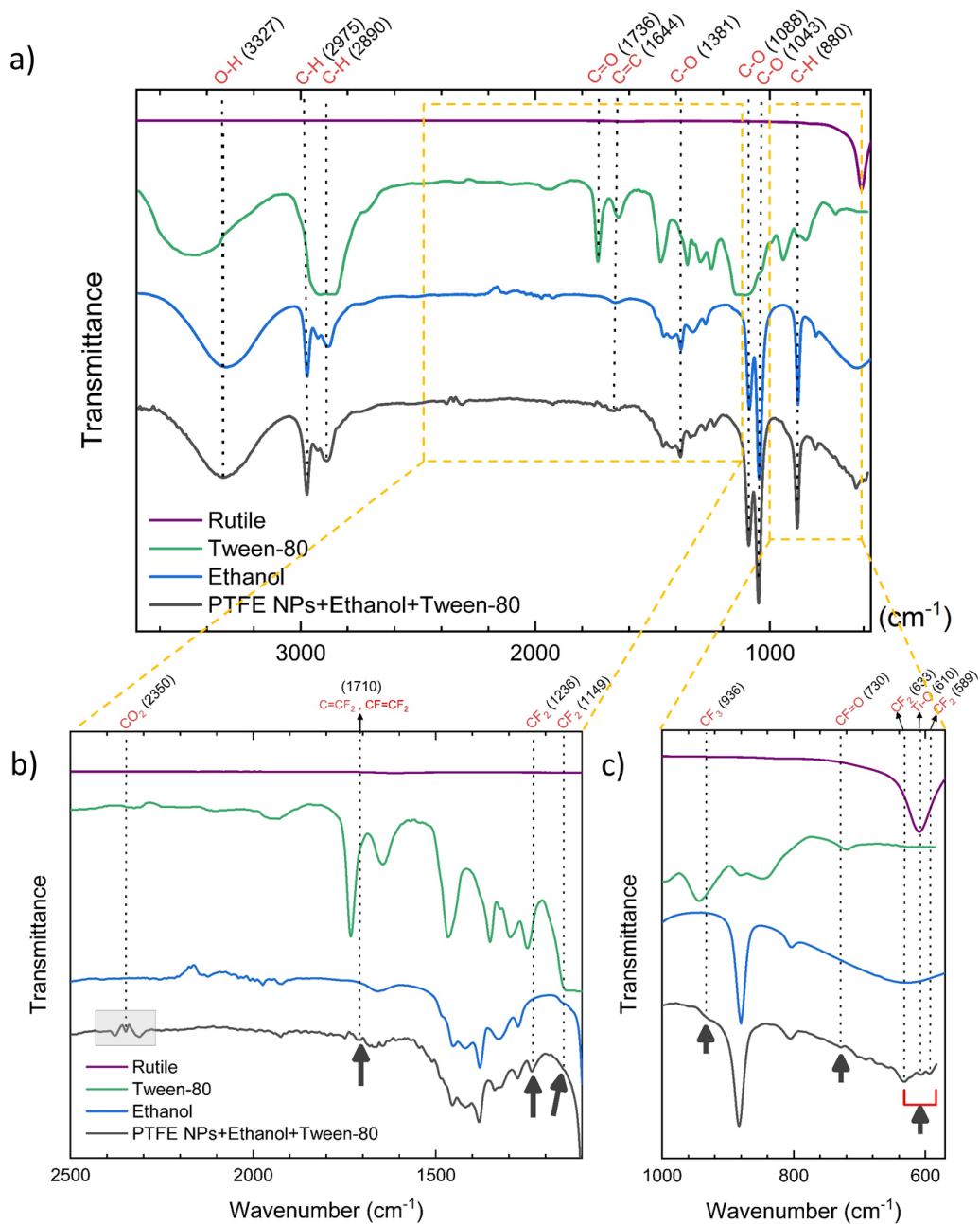


Figure 3.12: FTIR spectroscopy was carried out for the colloidal solution containing PTFE NPs. However, spectra for ethanol, Tween-80, and rutile were obtained from literature^{87,88} and digitizer for better comparison. The plots were normalized by using the intensity of O-H peak to obtain better results.

For FTIR of Tween-80, it is possible to observe the same peaks as ethanol with a small shift. However, an intense peak at 1736 cm^{-1} appears due to C=O stretching⁹⁸. The rutile (contamination) shows a small characteristic peak from stretching mode at 610 cm^{-1} , as shown in Figure 3.12 c)⁹⁹. A peak was identified at 2350 cm^{-1} whose frequency corresponds to an asymmetric stretching of CO_2 ⁹⁷, the carbon dioxide comes from the combustion of ethanol¹⁰⁰ during the sonication due to the high temperatures reached by the tip.

Chapter 4

Conclusions & Outlook

4.1 Conclusions

The production of PTFE fine-powder specified in the subsection 3.1.1, presents a dissimilar method to obtain it. The protocol established was designed after combining different sources of PTFE and solvents such as sprays, tapes, sealants, ethanol, methanol, isopropyl alcohol, or hydrofluoric acid. Different sources of PTFE, such as sprays, tapes and sealants, were employed to obtain the powder. Similarly, different solvents and acids were combined with the PTFE sources in order to obtain the powder. However, the best results were shown with “WEICONLOCK® AN 301-65 Pipe and Flange Sealing” and HF (38% - 40%). The PTFE obtained from this product was subjected to numerous washes in order to obtain the purest PTFE powder. However, the XRD pattern (Figure 3.5) displays the presence of contaminants. The contaminant was identified as rutile (TiO_2) thanks to the characteristic peaks observed in the same XRD pattern. In order to eliminate the contaminant (TiO_2), it is necessary to carry out more washes with HF as it dissolves TiO_2 and, once that the contaminant, is dissolved it can be removed from the PTFE by extracting the aqueous HF phase.

The PTFE NPs were made from the fine powder as shown in the protocol of subsection 3.1.2. The NPs were produced from the PTFE fine-powder by using ethanol as the solvent and Tween-80 as the surfactant. On one hand, the use of ethanol is based on the recommendation of Alexis Debut in ESPE, because this solvent is good to disperse polymers, which produce the best performance during TEM imaging. On the other hand, the surfactant Tween-80 is widely recognized for food, health, beauty, and medical uses. Therefore, Tween-80 was employed to stabilize the colloidal dispersion of PTFE NPs, demonstrating good

results as shown in TEM Figures 3.11. It is recommendable to employ a surfactant concentration of 1% (v/v) in order to avoid the formation of lipidic films that blur the TEM images. Finally, differential centrifugation proved to be good enough for obtaining NPs of homogeneous sizes, however there exists more technique to accomplish the same purpose. Differential centrifugation must be performed carefully to avoid the production of two population populations of NPs in the same sample. This mistake can be solved by manipulating carefully the tubes after each centrifugation. To sum up, the simplicity of these NPs allows the improvement of the protocol to obtain uniform sizes, because as nanoparticles become more complex in composition, the risk of variation increases proportionally.

The diffuse reflectance UV-Vis spectroscopy 3.2.1 indicates the range in which PTFE fine-powder absorbs (no-reflectance) electromagnetic radiation. After analysis, the fine-powder absorbs electromagnetic radiation for wavelengths lower than 410 nm, this powder can be employed when the absorbance of electromagnetic radiation such as ultraviolet or X-rays would be needed, for example sunscreens. Additionally, the transformation of the data to Kubelka-Munk was useful to point out the insulator properties of PTFE fine-powder with a band gap of 3.27 eV.

The XRD diffractogram, discussed in subsection 3.2.2, was analyzed using various methods to determine different parameters of the PTFE fine-powder. First, the sharp peaks denotes a crystalline structure; however, additional peaks were assigned to rutile contamination. The peaks of PTFE were analyzed and the results determined the hexagonal crystal (phase IV) structure of PTFE, this result is corroborated by the literature reported in Ref. 29, a phase IV present at room temperature. In addition, the analysis of crystallinity exhibit a good crystallinity of the powder that reaches 77.7%, where amorphous percentages are observed and assigned to amorphous phases I and II. Furthermore, the grain size was determined with the Scherrer equation whose results demonstrates that the fine powder has an average size of 36.02 nm. This means that the NPs bigger than 36.02 nm are originated due to agglomerations while smaller NPs can be produced due to fractures. Therefore, in order to produce NPs of homogeneous size, the sonication process must be optimized in order to break down the agglomerated particles without causing fractures in the crystals.

The X-ray attenuation of PTFE fine-powder was tested in subsection 3.2.3. The results obtained hold a lot of promise because the powder exhibits an extremely good attenuation of X-rays of different potentials and currents. Therefore, the fine-powder can be employed as a contrast agent for X-ray imaging as it attenuates tremendously the high energy radiation.

The PTFE fine-powder was subjected to US imaging as presented in subsection 3.2.4. The results observed are in good agreement with the literature, the as-obtained powder attenuating the US as shown in

Figures **a)** and **b)** of 3.9. Therefore, the PTFE fine-powder can be applied as contrast agent for ultrasound imaging.

Results from TEM, discussed in subsection 3.2.5, prove the existence of PTFE NPs as shown in Figure 3.11 that also points out that the concentration of 1% (v/v) of surfactant Tween-80 is enough to stabilize the NPs. Additionally, the effectiveness of differential centrifugation is denoted by comparing the images obtained before and after centrifuging in Figures 3.10 and 3.11. TEM images prior to centrifugation show large agglomerates, this indicates that the process of sonication must be improved by applying higher power and longer times to overcome the agglomerating forces, such as vdW, capillary or electrostatics. This is evidenced by the presence of two distinct populations of PTFE NPs according to the size in the sample.

FTIR analysis was performed in the colloidal dispersion of PTFE NPs, detailed in subsection 3.2.6. The FTIR spectrum of PTFE NPs in ethanol in the presence of Tween-80 exhibits characteristic peaks of PTFE, ethanol, and rutile. However, the peaks have not been shifted indicating, thus, the absence of bonds between the components confirming the assertion that PTFE is chemically inert due to the strong bond between C-F.

4.2 Outlook

The main objective of this project is to apply PTFE NPs for cancer hyperthermia treatment. The synthesis and characterization of the NPs have demonstrated additional potential applications for these NPs. PTFE is compatible with white blood cells in addition to its cytocompatibility and hemocompatibility making, thus, the as-produced PTFE NPs excellent candidates for several applications in the biomedical field. For example, the PTFE NPs can be used for cancer hyperthermia treatment using ultrasound as a source of energy owing to the fact PTFE NPs attenuate US with high efficiency increasing the temperature until 49 °C. At this temperature, cancer cells become more vulnerable to external factors, thus hyperthermia mediated with PTFE NPs combined with chemotherapy can attack malignant tumors more efficiently. Additionally, the PTFE NP-mediated hyperthermia treatment of cancer can be monitored in real-time either by X-ray or US imaging as PTFE attenuates both radiations.

Another potential application of the as-produced PTFE NPs lies in cancer treatment via radiotherapy. PTFE NPs can be used to monitor radiotherapy in real-time as this treatment employs X-rays which can affect healthy cells if the beam is not well focused. Moreover, this radiotherapy treatment can be monitored with X-ray imaging by exploiting the PTFE NPs as the contrast agent.

In the future, the PTFE NPs will be tested *in vitro* with cancer cell lines under a US source to determine their efficacy. This might will be followed by *in vivo* and biocompatibility tests on rats before envisaging moving to clinical trials should the tests be conclusive. In shorts, PTFE NPs hold a lot of promise!

Appendix

A.1 Abbreviations

Notation	Description
AMF	alternating magnetic field. 8, 19
CT	computerized tomography. 30
DNA	deoxyribonucleic acid. 1, 4, 6
DTGS	deuterated triglycine sulfate. 33
ePTFE	expanded polytetrafluoroethylene. 17, 18
ErbB2	tyrosine-protein kinase. 11
FTIR	Fourier-Transform Infrared spectroscopy. ix, 35
FWHM	full width at half maximum. 48
GNPs	gold nanoparticles. xii, 9–11
HCl	hydrochloric acid. 13
Her-GNPs	Herceptin-Gold nanoparticles. 10, 11
HF	hydrofluoric acid. ix, 12, 35, 36, 58
K-M	Kubelka Munk. 27, 40

Notation	Description
KHz	kilohertz. 16, 22
MHz	megahertz. 9, 16–19
MNPs	magnetic nanoparticles. 8
MRI	magnetic resonance imaging. 8, 30
NIR	near infrared. 9
NPs	nanoparticles. ix–xiii, 7–9, 11, 19–24, 35, 37, 38, 51, 54
NRU	Neutral Red Uptake. 14
PTFE	polytetrafluoroethylene. ix–xiv, 11–22, 35–41, 45–47, 49, 51, 54
RCF	relative centrifugal force. 24
RPM	revolutions per minute. 24, 36, 38
SiNPs	silicon nanoparticles. 9
SOLCA	Sociedad de Lucha Contra el Cáncer. 4, 5
SPR	surface plasmon resonance. 9
TEM	Transmission Electron Microscopy. ix, xii, 31, 32, 35, 49, 51
TFE	tetrafluoroethylene. 12, 13
Tween-80	polysorbate 80. ix
US	ultrasound. ix, 6, 8, 9, 16, 19, 23, 30
UV-Vis	ultraviolet visible spectroscopy. ix, xi, xiv, 35, 39, 40
vdW	van der Waals. 22, 52, 60

Notation	Description
W	watt. 17
WHO	World Health Organization. 3
XRD	X-ray diffraction. ix, xii, xiv, 11, 28, 35, 46, 47

Bibliography

- [1] Weinberg, R. In *The Biology of Cancer*; Science, G., Ed.; Garland Science, Taylor Francis Group, LLC, 2014; pp 31–70.
- [2] Sinden, R. In *DNA Structure and Function*; Press, A., Ed.; Academic Press, Inc., 1994; pp 1–56.
- [3] Lodish, H.; Berk, H.; Zipursky, S. L.; Matsudaira, P.; Baltimore, D.; Darnell, J. In *Molecular Cell Biology*; Freeman, W. H., Ed.; W. H. Freeman, 2000; Vol. 5th ed.; pp 351–404.
- [4] Weinberg, R. In *The Biology of Cancer*; Science, G., Ed.; Garland Science, Taylor Francis Group, LLC, 2014; pp 1–29.
- [5] De Visser, K. E.; Eichten, A.; Coussens, L. M. Paradoxical roles of the immune system during cancer development. *Nature Reviews Cancer* **2006**, *6*, 24–37.
- [6] Mitchell, M. G. In *Cell Biology*; Mitchell, M. G., Ed.; Academic Press: Boston, 2016; pp 1–119.
- [7] Bray, F.; Ferlay, J.; Soerjomataram, I.; Siegel, R. L.; Torre, L. A.; Jemal, A. Global cancer statistics 2018: GLOBOCAN estimates of incidence and mortality worldwide for 36 cancers in 185 countries. *CA: a cancer journal for clinicians* **2018**, *68*, 394–424.
- [8] Romano, M. E.; Diorio, O. J.; Chamberlin, M. D. In *Cancer and Society: A Multidisciplinary Assessment and Strategies for Action*; Bernicker, E. H., Ed.; Springer International Publishing: Cham, 2019; pp 27–38.
- [9] Kelsh, M. A.; Morimoto, L.; Lau, E. Cancer mortality and oil production in the Amazon Region of Ecuador, 1990-2005. *International Archives of Occupational and Environmental Health* **2009**, *82*, 381–95.

- [10] Hurtig, A. K.; San Sebastián, M. Incidence of childhood leukemia and oil exploitation in the Amazon basin of Ecuador. *International Journal of Occupational and Environmental Health* **2004**, *10*, 245–50.
- [11] Ecuador (Cancer Profile). 2015; https://www.who.int/cancer/country-profiles/ecu_en.pdf.
- [12] Chauhan, V. P.; Stylianopoulos, T.; Martin, J. D.; Popovič, Z.; Chen, O.; Kamoun, W. S.; Bawendi, M. G.; Fukumura, D.; Jain, R. K. Normalization of tumour blood vessels improves the delivery of nanomedicines in a size-dependent manner. *Nature Nanotechnology* **2012**, *7*, 383–388.
- [13] Misra, R.; Acharya, S.; Sahoo, S. K. Cancer nanotechnology: Application of nanotechnology in cancer therapy. *Drug Discovery Today* **2010**, *15*, 842–50.
- [14] Weinberg, R. *The Biology of Cancer*; Garland Science, Taylor Francis Group, LLC, 2014; pp 797–875.
- [15] Sociedad de Lucha Contra el Cáncer. n.d.; <https://www.solca.med.ec/>.
- [16] Sawyers, C. Targeted cancer therapy. *Nature* **2004**, *432*, 294–297.
- [17] Clarke, M. F.; Hass, A. T. *Reviews in Cell Biology and Molecular Medicine*; American Cancer Society, 2006; pp 221–236.
- [18] Blattman, J. N.; Greenberg, P. D. Cancer immunotherapy: A treatment for the masses. *Science* **2004**, *305*, 200–5.
- [19] Dong, H.; Markovic, S. *The basics of cancer immunotherapy*; Springer International Publishing, 2018; pp 21–33.
- [20] Hahn, G. *Hyperthermia and Cancer*; Springer US, 2012; pp 1–6.
- [21] Nijhawan, G.; Nijhawan, S. S.; Sethi, M. In *Noble Metal-Metal Oxide Hybrid Nanoparticles*; Mohapatra, S., Nguyen, T. A., Nguyen-Tri, P., Eds.; Micro and Nano Technologies; Woodhead Publishing, 2019; pp 241 – 263.
- [22] Wust, P.; Hildebrandt, B.; Sreenivasa, G.; Rau, B.; Gellermann, J.; Riess, H.; Felix, R.; Schlag, P. Hyperthermia in combined treatment of cancer. *Lancet Oncology* **2002**, *3*, 487–97.

- [23] Chatterjee, D. K.; Diagaradjane, P.; Krishnan, S. Nanoparticle-mediated hyperthermia in cancer therapy. *Therapeutic delivery* **2011**, *2*, 1001–14.
- [24] Hahn, G. *Hyperthermia and Cancer*; Springer US, 2012; pp 131–176.
- [25] Sviridov, A. P.; Osminkina, L. A.; Kharin, A. Y.; Gongansky, M. B.; Kargina, J. V.; Kudryavtsev, A. A.; Bezsudnova, Y. I.; Perova, T. S.; Geloen, A.; Lysenko, V.; Timoshenko, V. Y. Cytotoxicity control of silicon nanoparticles by biopolymer coating and ultrasound irradiation for cancer theranostic applications. *Nanotechnology*
- [26] Pérez-Hernández, M. In *Nanomaterials for Magnetic and Optical Hyperthermia Applications*; Fratila, R. M., Fuente, J. M. D. L., Eds.; Micro and Nano Technologies; Elsevier, 2019; pp 201–228.
- [27] Shibaguchi, H.; Tsuru, H.; Kuroki, M.; Kuroki, M. Sonodynamic cancer therapy: A non-invasive and repeatable approach using low-intensity ultrasound with a sonosensitizer. **2011**, *31*, 2425–9.
- [28] Jiang, W.; Kim, B. Y.; Rutka, J. T.; Chan, W. C. Nanoparticle-mediated cellular response is size-dependent. *Nature Nanotechnology* **2008**, *3*, 145–150.
- [29] Brown, E. N.; Clausen, B.; Brown, D. W. In situ measurement of crystalline lattice strains in phase IV polytetrafluoroethylene. *Journal of Neutron Research* **2007**, *15*, 139–146.
- [30] Dargaville, T. R.; George, G. A.; Hill, D. J.; Whittaker, A. K. High energy radiation grafting of fluoropolymers. *Progress in Polymer Science (Oxford)* **2003**, *28*, 1355–1376.
- [31] Risbud, M. V.; Hambir, S.; Jog, J.; Bhonde, R. Biocompatibility assessment of polytetrafluoroethylene/wollastonite composites using endothelial cells and macrophages. *Journal of Biomaterials Science, Polymer Edition* **2001**, *12*, 1177–89.
- [32] Noda, Y.; Hosokawa, K.; Mizuno, T.; Ihara, K.; Shimizu, T. Polytetrafluoroethylene fine particles and powder. 1990; US5324785A, United States.
- [33] Ebnesajjad, S., Ed. *Introduction to Fluoropolymers*; William Andrew Publishing: Oxford, 2013; pp 91 – 124.
- [34] Nakajima, K.; Bell, A. T.; Shen, M.; Millard, M. M. Plasma polymerization of tetrafluoroethylene. *Journal of Applied Polymer Science* **1979**, *108*, 163–179.

- [35] Romack, T. J.; Kipp, B. E.; DeSimone, J. M. Polymerization of Tetrafluoroethylene in a Hybrid Carbon Dioxide/Aqueous Medium. *Macromolecules* **1995**, *28*, 8432–8434.
- [36] Kim, C. U.; Lee, J. M.; K. Ihm, S. Emulsion polymerization of tetrafluoroethylene: Effects of reaction conditions on particle formation. *Journal of Fluorine Chemistry* **1999**, *96*, 11–21.
- [37] Drobny, J. In *Specialty Thermoplastics*; Drobny, J., Ed.; Springer Berlin Heidelberg: Berlin, Heidelberg, 2015; pp 1–4.
- [38] Drobny, J. In *Specialty Thermoplastics*; Drobny, J., Ed.; Springer Berlin Heidelberg: Berlin, Heidelberg, 2015; pp 5–9.
- [39] Blair C., C.; Quinn, B. *Microplastic Pollutants*; 2017; pp 57–100.
- [40] Biswas, S. K.; Vijayan, K. Friction and wear of PTFE - a review. *Wear* **1992**, *158*, 193–211.
- [41] Mahajan, S. D.; Law, W.-C.; Aalinkeel, R.; Reynolds, J.; Nair, B. B.; Yong, K.-T.; Roy, I.; Prasad, P. N.; Schwartz, S. A. In *Nanomedicine*; Düzgüneş, N., Ed.; Methods in Enzymology; Academic Press, 2012; Vol. 509; pp 41–60.
- [42] Melo, P. S.; Maria, S. S.; Vidal, B. C.; Haun, M.; Durán, N. Violacein cytotoxicity and induction of apoptosis in V79 cells. *In vitro cellular & developmental biology. Animal* **2000**, *36*, 539–43.
- [43] Lackie, J. In *The Dictionary of Cell Molecular Biology (Fifth Edition)*, fifth edition ed.; Lackie, J., Ed.; Academic Press: Boston, 2013; pp 361 – 388.
- [44] Zhang, J.; Li, J.; Han, Y. Superhydrophobic PTFE surfaces by extension. *Macromolecular Rapid Communications* **2004**, *25*, 1105–1108.
- [45] Du, C.; Wang, J.; Chen, Z.; Chen, D. Durable superhydrophobic and superoleophilic filter paper for oil-water separation prepared by a colloidal deposition method. *Applied Surface Science* **2014**, *313*, 304–310.
- [46] Lau, K. K. S.; Bico, J.; Teo, K. B. K.; Chhowalla, M.; Amaratunga, G. A. J.; Milne, W. I.; McKinley, G. H.; Gleason, K. K. Superhydrophobic Carbon Nanotube Forests. *Nano Letters* **2003**, *3*, 1701–1705.

- [47] Kannan, R. Y.; Salacinski, H. J.; Butler, P. E.; Hamilton, G.; Seifalian, A. M. Current status of prosthetic bypass grafts: A review. *Journal of Biomedical Materials Research - Part B Applied Biomaterials* **2005**, *74*, 570–81.
- [48] Klinkert, P.; Post, P. N.; Breslau, P. J.; van Bockel, J. H. Saphenous vein versus PTFE for above-knee femoropopliteal bypass. A review of the literature. *European Journal of Vascular and Endovascular Surgery* **2004**, *27*, 357–62.
- [49] Nishida, K.; Sakaguchi, H.; Xie, P.; Terasawa, Y.; Ozawa, M.; Kamei, M.; Nishida, K. Biocompatibility and durability of Teflon-coated platinum-iridium wires implanted in the vitreous cavity. *Journal of Artificial Organs* **2011**, *14*, 357–63.
- [50] Roy-Chaudhury, P.; Sukhatme, V. P.; Cheung, A. K. Hemodialysis Vascular Access Dysfunction: A Cellular and Molecular Viewpoint. *Journal of the American Society of Nephrology* **2006**, *17*, 1112–27.
- [51] Weidner, V. R.; Hsia, J. J. Reflection properties of pressed polytetrafluoroethylene powder. *Journal of the Optical Society of America* **2008**, *71*, 856–861.
- [52] Koizumi, S.; Ichiba, S.; Simizu, T.; Okuno, C.; Kadowaki, T.; Yamamoto, K. Polytetrafluoroethylene fine powder and process for producing the same. 1976; US4159370A, United States.
- [53] Musolf, K.; Penn, D. J. In *Evolution of the House Mouse*; Macholán, M., Baird, S. J. E., Munclinger, P., PiÅąlek, J., Eds.; Cambridge Studies in Morphology and Molecules: New Paradigms in Evolutionary Bio; Cambridge University Press, 2012; pp 253–277.
- [54] Reilly, R. M. In *Medical Imaging for Health Professionals: Technologies and Clinical Applications*; Reilly, R. M., Ed.; John Wiley Sons, 2019; pp 107–113.
- [55] Jiang, X.; Savchenko, O.; Li, Y.; Qi, S.; Yang, T.; Zhang, W.; Chen, J. A Review of Low-Intensity Pulsed Ultrasound for Therapeutic Applications. *IEEE Transactions on Biomedical Engineering* **2018**, *PP*, 1–1.
- [56] Farnsworth, T.; Egres, R. Expanded polytetrafluoroethylene (ePTFE)-reinforced perfluoroelastomers (FFKM). 2012; US20030211264A1, United States.

- [57] Brinton, M. R.; Stewart, R. J.; Cheung, A. K.; Christensen, D. A.; Shiu, Y. T. E. Modelling ultrasound-induced mild hyperthermia of hyperplasia in vascular grafts. *Theoretical Biology and Medical Modelling* **2011**, *3*, 42.
- [58] Vickers, D. B. Hyperthermia for treatment of hyperplasia in a hemodialysis access graft. Ph.D. thesis, 2008.
- [59] Taurozzi, J. S.; Hackley, V. A.; Wiesner, M. R. Ultrasonic dispersion of nanoparticles for environmental, health and safety assessment issues and recommendations. *Nanotoxicology* **2011**, *5*, 711–729.
- [60] Robertson, J. D.; Rizzello, L.; Avila-Olias, M.; Gaitzsch, J.; Contini, C.; Magoń, M. S.; Renshaw, S. A.; Battaglia, G. Purification of Nanoparticles by Size and Shape. *Scientific Reports* **2016**, *6*, 27494.
- [61] Thomason, Differentielle Zentrifugation. 2009; https://en.wikipedia.org/wiki/Differential_centrifugation#/media/File:Differentielle_zentrifugation.png.
- [62] Clarjke, P. Theory of sedimentation and centrifugation. 2009; Document online: <http://collect.org.uk/icenimsg/pollensuspension-2.pdf>.
- [63] Ultraviolet - Visible Spectroscopy (UV). *Advancing the Chemical Sciences* **2009**,
- [64] Blitz, J. P.; Mirabella, F. M. In *Modern Techniques in Applied Molecular Spectroscopy*; Mirabella, F. M., Ed.; John Wiley Sons, 1998; pp 185–219.
- [65] What is Kubelka-Munk? n.d.; <https://mmrc.caltech.edu/FTIR/Literature/DiffReflectance/Kubelka-Munk.pdf>, Harrick Scientific Products, Inc.
- [66] Waseda, Y.; Matsubara, E.; Shinoda, K. *X-Ray Diffraction Crystallography: Introduction, Examples and Solved Problems*; Springer Berlin Heidelberg: Berlin, Heidelberg, 2011; pp 67–106.
- [67] Chatterjee, A. In *Handbook of Analytical Techniques in Concrete Science and Technology*; Ramachandran, V., Beaudoin, J. J., Eds.; William Andrew Publishing: Norwich, NY, 2001; pp 275 – 332.
- [68] Sima, F.; Ristoscu, C.; Duta, L.; Gallet, O.; Anselme, K.; Mihailescu, I. In *Laser Surface Modification of Biomaterials*; Vilar, R., Ed.; Woodhead Publishing, 2016; pp 77 – 125.

- [69] Yue, G. Z.; Qiu, Q.; Gao, B.; Cheng, Y.; Zhang, J.; Shimoda, H.; Chang, S.; Lu, J. P.; Zhou, O. Generation of continuous and pulsed diagnostic imaging x-ray radiation using a carbon-nanotube-based field-emission cathode. *Applied Physics Letters* **2002**, *81*, 355–357.
- [70] Lotto, C. In *Single-Photon Imaging*; Seitz, P., Theuwissen, A. J., Eds.; Springer Berlin Heidelberg: Berlin, Heidelberg, 2011; pp 249–274.
- [71] Shung, K. K. *Diagnostic Ultrasound: Imaging and Blood Flow Measurements*; CRC Press, 2005; pp 1–3.
- [72] Wells, P. N. T. Ultrasound imaging. *Physics in Medicine and Biology* **2006**, *51*, R83–R98.
- [73] Wei, X. Q.; Zhang, Z.; Yu, Y. X.; Man, B. Y. Comparative study on structural and optical properties of ZnO thin films prepared by PLD using ZnO powder target and ceramic target. *Optics and Laser Technology* **2009**, *41*, 530–534.
- [74] Williams, D. B.; Carter, C. B. *Transmission Electron Microscopy: A Textbook for Materials Science*; Springer US: Boston, MA, 2009; pp 3–22.
- [75] Faix, O. In *Methods in Lignin Chemistry*; Lin, S. Y., Dence, C. W., Eds.; Springer Berlin Heidelberg: Berlin, Heidelberg, 1992; pp 83–213.
- [76] Bardwell, J. A.; Dignam, M. J. In *Fourier Transform Infrared Characterization of Polymers*; Ishida, H., Ed.; Springer US: Boston, MA, 1987; pp 415–443.
- [77] Coleman, C. A.; Rose, J. G.; Murray, C. J. General Acid Catalysis of the Reduction of p-Benzoquinone by an NADH Analog. Evidence for Concerted Hydride and Hydron Transfer. *Journal of the American Chemical Society* **1992**, *114*, 9755–9762.
- [78] Escobedo A. Morales, E. Sanchez Mora, U. P. Use of diffuse reflectance spectroscopy for optical characterization of un-supported nanostructures. *REVISTA MEXICANA DE FÍSICA* **2007**, *53*, 78.
- [79] Cohen-Tannoudji, C.; Diu, B.; Franck, L. *Quantum mechanics*; Wiley, 1991; pp 7–88.
- [80] Hayt, W. H.; Buck, J. A.; undefined, u. u. In *Engineering electromagnetics*; Co., M.-H. P., Ed.; Mindanao State University, 2001; pp 119–168.
- [81] Elton, L. R. B.; Jackson, D. F. X-Ray Diffraction and the Bragg Law. *American Journal of Physics* **1966**, *34*, 1036.

- [82] Waseda, Y.; Matsubara, E.; Shinoda, K. *X-Ray Diffraction Crystallography: Introduction, Examples and Solved Problems*; Springer Berlin Heidelberg: Berlin, Heidelberg, 2011; pp 21–66.
- [83] Lebedev, Y. A.; Korolev, Y. M.; Polikarpov, V. M.; Ignat'eva, L. N.; Antipov, E. M. X-ray powder diffraction study of polytetrafluoroethylene. *Crystallography Reports* **2010**, *55*, 609–614.
- [84] Rae, P. J.; Dattelbaum, D. M. The properties of poly(tetrafluoroethylene) (PTFE) in compression. *Polymer* **2004**, *45*, 7615–7625.
- [85] Patterson, A. L. The scherrer formula for X-ray particle size determination. *Physical Review* **1939**, *56*, 978.
- [86] Singh, A. K. In *Advanced x-ray techniques in research and industry*; Singh, D. A. K., Ed.; IOS Press, 2005; pp 268–286.
- [87] WYANDOTTE CHEMICALS CORP., WYANDOTTE, MICHIGAN, USACOBLENTZ SOCIETY, SORBITAN MONO-OLEATE. data retrieved from NIST, <https://webbook.nist.gov/cgi/cbook.cgi?ID=C1338438&Mask=80#IR-Spec>, CAS: 1338-43-8, 1970.
- [88] Database of ATR-FT-IR spectra of various materials Institute of Chemistry University of Tartu, Estonia, ATR-FT-IR spectrum of Ethanol (4000 - 225 cm⁻¹). data retrieved from Database of ATR-FT-IR spectra of various materials, http://lisa.chem.ut.ee/IR_spectra/conservation_materials/ethanol/, 2015.
- [89] Gemological Institute of America RRUF, Rutile. data retrieved from RRUFF, <http://rruff.info/Rutile/R110109>, RRUFF ID: R110109, 2010.
- [90] Satulu, V.; Ionita, M. D.; Vizireanu, S.; Mitu, B.; Dinescu, G. Plasma processing with fluorine chemistry for modification of surfaces wettability. *Molecules* **2016**, *21*, 1711–1726.
- [91] Wang, H.; Wen, Y.; Peng, H.; Zheng, C.; Li, Y.; Wang, S.; Sun, S.; Xie, X.; Zhou, X. Grafting polytetrafluoroethylene micropowder via in situ electron beam irradiation-induced polymerization. *Polymers* **2018**, *10*, 503.
- [92] Zhang, Y.; Yang, B.; Li, K.; Hou, D.; Zhao, C.; Wang, J. Electrospun porous poly(tetrafluoroethylene-co-hexafluoropropylene-co-vinylidene fluoride) membranes for membrane distillation. *RSC Advances* **2017**, *7*, 56183–56193.

- [93] Hunke, H.; Soin, N.; Shah, T.; Kramer, E.; Pascual, A.; Karuna, M.; Siores, E. Low-Pressure H₂, NH₃ Microwave Plasma Treatment of Polytetrafluoroethylene (PTFE) Powders: Chemical, Thermal and Wettability Analysis. *Materials* **2015**, *8*, 2258–2275.
- [94] Abdul mudalip, S. k.; Abu Bakar, M. R.; Adam, F.; Jamal, P. Structures and Hydrogen Bonding Recognition of Mefenamic Acid Form I Crystals in Mefenamic Acid/Ethanol Solution. *International Journal of Chemical Engineering and Applications* **2013**, *4*, 124–128.
- [95] Lu, J.; Hai, W.; Meng, J.; Ren, S. In *Progress in Green Tribology*; Davim, J. P., Ed.; Walter de Gruyter GmbH Co KG, 2017; pp 65–72.
- [96] Liu, Y.; Gu, J.; Zhang, J.; Yu, F.; Wang, J.; Nie, N.; Li, W. LiFePO₄ nanoparticles growth with preferential (010) face modulated by Tween-80. *RSC Adv.* **2015**, *5*, 9745–9751.
- [97] Schriver, A.; Schriver-Mazzuoli, L.; Ehrenfreund, P.; D’Hendecourt, L. One possible origin of ethanol in interstellar medium: Photochemistry of mixed CO₂-C₂H₆ films at 11 K. A FTIR study. *Chemical Physics* **2007**, *334*, 128–137.
- [98] Macher, T.; Sherwood, J.; Xu, Y.; Lee, M.; Dennis, G.; Qin, Y.; Daly, D.; Swatloski, R.; Bao, Y. **2015**, *16*, 1–8.
- [99] Kakuma, Y.; Nosaka, A. Y.; Nosaka, Y. Difference in TiO₂ photocatalytic mechanism between rutile and anatase studied by the detection of active oxygen and surface species in water. *Physical Chemistry Chemical Physics* **2015**, *17*, 18691–18698.
- [100] Marland, G.; Turhollow, A. F. CO₂ emissions from the production and combustion of fuel ethanol from corn. *Energy* **1991**, *16*, 1307–1316.